

Article

Analysis of the Selected Design Changes in a Wheel Hub Motor Electromagnetic Circuit on Motor Operating Parameters While Car Driving

Piotr Dukalski ^{1,*}  and Roman Krok ² 

¹ Centre of Electrical Drives and Machines, Łukasiewicz Research Network—Upper Silesian Institute of Technology, Str. K. Miarki 12-14, 44-100 Gliwice, Poland

² Department of Mechatronics, Faculty of Electrical Engineering, Silesian University of Technology, 44-100 Gliwice, Poland; roman.krok@polsl.pl

* Correspondence: piotr.dukalski@git.lukasiewicz.gov.pl

Abstract: The drive system of an electric car must meet road requirements related to overcoming obstacles and driving dynamics depending on the class and purpose of the vehicle. The driving dynamics of modern cars as well as size and weight limitations mean that wheel hub motors operate with relatively high current density and high power supply frequency, which may generate significant power losses in the windings and permanent magnets and increase their operating temperature. Designers of this type of motor often face the need to minimize the motor's weight, as it constitutes the unsprung mass of the vehicle. Another limitation for motor designers is the motor dimensions, which are limited by the dimensions of the rim, the arrangement of suspension elements and the braking system. The article presents two directions in the design of wheel hub motors. The first one involves minimizing the length of the stator magnetic core, which allows for shortening of the axial dimension and mass of the motor but involves increasing the thermal load and the need for deeper de-excitation. The second one involves increasing the number of pairs of magnetic poles, which reduces the mass, increases the internal diameter of the motor and shortens the construction of the fronts, but is associated with an increase in the motor operating frequency and increased power losses. Additionally, increasing the number of pairs of magnetic poles is often associated with reducing the number of slots per pole and the phase for technological reasons, which in turn leads to a greater share of spatial harmonics of the magnetomotive force in the air gap and may lead to the generation of higher power losses and higher operating temperatures of permanent magnets. The analysis is based on a simulation of the motor operation, modeled on the basis of laboratory tests of the prototype, while the car is driving in various driving cycles.

Keywords: wheel hub motor; electric drive; permanent magnet synchronous motor; electric car



Citation: Dukalski, P.; Krok, R. Analysis of the Selected Design Changes in a Wheel Hub Motor Electromagnetic Circuit on Motor Operating Parameters While Car Driving. *Energies* **2024**, *17*, 6091. <https://doi.org/10.3390/en17236091>

Academic Editor: Frede Blaabjerg

Received: 29 October 2024

Revised: 26 November 2024

Accepted: 29 November 2024

Published: 3 December 2024



Copyright: © 2024 by the authors. Licensee MDPI, Basel, Switzerland. This article is an open access article distributed under the terms and conditions of the Creative Commons Attribution (CC BY) license (<https://creativecommons.org/licenses/by/4.0/>).

1. Introduction

The use of wheel hub motors in cars opens up a number of new technical possibilities for the automotive industry. This solution allows for the development of new concepts for the drive units themselves but also brings about new possibilities for designing the shape of the car or the arrangement of its interior. The new technical possibilities of this solution result primarily from the elimination of all intermediary mechanisms used to transmit torque between the motor and the wheel, such as differentials, drive axles, drive shafts and gears.

In addition, the decentralization of the drive, which takes place in the case of electric motors installed in wheel hubs, enables new functionalities regarding vehicle dynamics due to direct control of the torque of each drive wheel separately. Decentralization of the drive also allows for the introduction of electrodynamic forms of advanced steering support systems, e.g., ABS, electronic stabilization system (ESP), or TCS (traction control system).

The main advantages of using electric motors for installation in the wheels of electric vehicles are presented below:

- Eliminating elements intermediating the transmission of torque reduces the vehicle's weight by eliminating the weight of the transmission, axle shafts and differential, which translates into energy consumption and, as a result, increases the vehicle's range.
- Increases the efficiency of the system due to the elimination of intermediary mechanisms, which themselves are characterized by power losses and whose efficiency, depending on the gear, may vary even in the range of 96% to 76% in the case of multi-speed gearboxes [1].
- Provides additional space in the vehicle body that can be used to increase the cargo area or install an additional battery, fuel cells or other components, e.g., inverters. Another possibility is to optimize the crumple zone.
- Elements that transmit torque are sources of noise, vibration and so-called "drive hardness" while driving [2,3]. Their elimination increases the driver's comfort when using the vehicle.
- Creation of new possibilities in the field of car control due to direct control of the torque of each of the vehicle's wheels. This solution ensures greater driving dynamics and is less susceptible to vibrations during load changes compared to central drives with a gear, clutch and drive shaft. It also allows for cooperation with vehicle steering support systems—ABS, ESP and TCS [4].
- Elimination of mechanical intermediary elements allows for the simplification of the design of the drive system itself and a reduction in their maintenance costs [4].
- Regenerative braking can be more effective due to the lack of intermediate elements and associated power losses.
- Direct drives guarantee the modularity of the design of drive units because they are relatively easy to implement in various types of vehicles based on drives with a different number of electric motors.
- Elimination of the centrally mounted electric motor under the hood of the car and elements mediating the transmission of torque allows for the design of more aerodynamic vehicle shapes.
- Disassembly when servicing or replacing the motor is relatively easy.
- The use of electric drive motors in wheels allows for the development of new hybrid drive structures. The combustion engine can be supported by electric motors built into the wheels in various operating modes, such as the following:
 - Only electric drive in "green zones" of cities;
 - Support when driving on difficult terrain (overcoming obstacles, acceleration, starting when driving outside zones closed to combustion cars);
 - Regenerative braking and support for vehicle control systems when driving outside zones closed to combustion cars.

Wheel hub motors perfectly fit into a number of current trends in the development of drives and electric traction motors:

- (a) Improvement of motors installed in the wheels of cars and commercial vehicles;
- (b) Increasing the power density in electric traction motors;
- (c) Development of integrated drive units, e.g., motors with gears, motors with drive axles;
- (d) Drive modularity and drive scalability;
- (e) Evaluation of vehicle architecture and structure;
- (f) Universal platforms combining the needs of passenger transport and goods transport and special applications;
- (g) Modular drive axles with innovative cooling system concepts;
- (h) Heat transfer and control strategies for each cooled component of the motor, inverter and battery;
- (i) Increasing the efficiency of electric motors and the scope of regenerative braking.

The mentioned directions of development of electric drives and motors aim to develop compact, integrated solutions that will ensure flexibility in the use of drives in vehicles for various purposes and will result in savings in the production of electric vehicles.

Compared to the central drive used, solutions based on electric motors in wheel hubs have a number of challenges/disadvantages that make it difficult to implement this type of drive unit in cars:

- Challenges related to the design of drive motors in wheel hubs:
 - Problems with heat dissipation;
 - Dimension limitations of the motor (rim dimensions, location of suspension and braking system elements);
 - The need to limit the motor weight, which constitutes the unsprung mass of the vehicle;
 - The need to seal the motor.
- The need to develop a new control system and cooperation with vehicle steering support systems—ABS, ESP and TCS.
- Increasing the number of inverters, which increase costs; in addition, these must be properly located, preferably close to the motor and drive wheel.
- More extensive cooling system. The coolant circuit must include more components, including up to four inverters and four motors;
- More extensive power supply system covering 2–4 drives.
- Development of a new vehicle protection system against failure of the drive unit.
- The need to strengthen the elements of the suspension and shock absorption system.
- High costs and risks of entering the car market:
 - The automotive market is restrictive and is based on a number of standards related to the reliability and safety of vehicle use, and the discussed solution of motors and control systems, especially for the automotive market, is in the development stage.
 - The limited number of manufacturers of this type of motors poses a risk related to the lack of diversification of sub-suppliers.
 - Limited number of specialists experienced in this area.
 - Very high costs of entering the market (related to global training of specialists, technicians and service technicians).
 - Limited possibilities based on developed technologies, which in the case of the automotive industry is a major disadvantage due to high initial costs and the costs of risk incurred. Risk, from the perspective of project management, is the result of probability and losses incurred in the event of its occurrence. It is difficult to introduce such a solution gradually because the change affects the entire drive topology and related technologies and design strategies of the entire vehicle.

If the driving characteristics of cars with wheel hub motors are to be comparable to those of cars with combustion motors or cars with a centrally mounted electric motor with a gearbox, the wheel hub motors must have a sufficiently high maximum torque. This is necessary to guarantee the required acceleration or overcome obstacles such as curbs. Overcoming the resistance to vehicle movement while driving at maximum speed also requires a sufficiently large torque. It is important to provide the possibility of long-term overload torque so that the vehicle can move at the required speed on slopes and climbs. The most popular motors currently used for installation in wheel hubs, due to their high power density in relation to their weight, are motors excited by permanent magnets [5–14]. In their case, a very difficult problem that must be solved by the designer and constructor is maintaining the temperature of the elements (especially the winding and magnets) at a level not exceeding the permissible value. The topic of thermal calculations of electric motors excited by permanent magnets is the subject of many research works [14–25]. Additionally, the motor of such an application should be designed to reduce cogging torque and torque ripple [26–34].

The design guidelines set very high requirements for the operating parameters of the electric motor while maintaining its very low weight. The ratio of the sprung mass to the unsprung mass of the vehicle is important. This problem has been described in many publications [35–46]. Research is being carried out to introduce design changes aimed at using the motor mass in the construction of the vibration absorber [47], or using a special motor structure to transform the unsprung mass of the stator into a sprung mass [48,49]. For example, it was proposed to convert the unsprung mass of the motor in the wheel into sprung mass by using an additional vibration-reducing mechanism that can be installed in parallel with the suspension system. Some research works focus on the suspension system and control system for drives with motors in vehicle wheels [50–52]. The wheel hub motors of modern electric cars are relatively low-speed motors compared to their full-gear, mid-mounted counterparts. Their maximum rotational speed usually reaches $n = 1500$ rpm [53]. Designers of this type of motor are often forced to reduce the motor's weight and adapt its overall dimensions to the rim diameter, axial length (due to the arrangement of suspension system elements and the braking system) and internal diameter (due to adaptation to the drum brake and brake system). The article presents two directions in the design of electromagnetic circuits of this type of motor. The first one involves shortening the length of the motor's magnetic core. The second is to increase the number of magnetic poles.

The article aims to present the impact of design changes in the electromagnetic circuit on the operating parameters of the wheel hub motor operating in a car. Publications dealing with this type of considerations are usually based on selected work points, or on work characteristics. This does not provide a complete practical view, especially since these are electric motors with a compact design, which are very limited in size, and which must operate in a wide operating range to meet the requirements of the diverse driving dynamics of a modern car.

When constructors introduce design changes to the motor's electromagnetic circuit, the range of generated torque has to cover the required driving dynamics of the car in which the motors operate. Other conditions that must be met are thermal requirements. During operation forced by the driving dynamics of the car, the motor should not exceed the operating temperatures of elements that may be damaged. Such elements may be winding insulation, slot insulation, epoxy resin used for encapsulation and permanent magnets. Additionally, the permissible operating temperature of permanent magnets depends on the influence of the external magnetic field, the flux of which is directed opposite to the magnetic flux from the magnet. This situation occurs when the motor is operating in the second control zone, the field weakening zone.

When redesigning the motor's electromagnetic circuit, it seems to be very interesting for the designer to analyze how the temperatures and power losses generated in individual elements will change during various car driving scenarios, especially since power losses in individual elements of the electromagnetic circuit depend on the following variables that change while the car is driving: current density, operating frequency, element temperature and the influence of field weakening.

The article presents a computational model in the ANSYS Motor CAD program (V15.1.7). The model incorporates three models, including a coupled model of the electromagnetic circuit with a thermal model. These models were calibrated based on laboratory tests on a manufactured wheel hub motor prototype and from the car model, which allows us to determine the requirements for the operating parameters of the electric motor. The developed models were used to simulate the operation of the wheel hub motor in driving cycles that represent the average driving dynamics of a car in real scenarios, such as driving in the city or driving on the highway.

2. Computational Model

Wheel hub motors are often designed as multi-pole electric motors with an external rotor. This is due to the space limitation, the structure of the rim and wheel mounting elements in the wheel and the best use of space for the electromagnetic circuit. The

electromagnetic circuit of such a motor is toroidal, so that space found inside this toroid may be used. The cross-section of the three-dimensional (3D) model of the discussed SMzs200S32 (Manufactured by Łukasiewicz Research Network—Upper Silesian Institute of Technology, Gliwice, Poland) motor is shown in Figure 1.

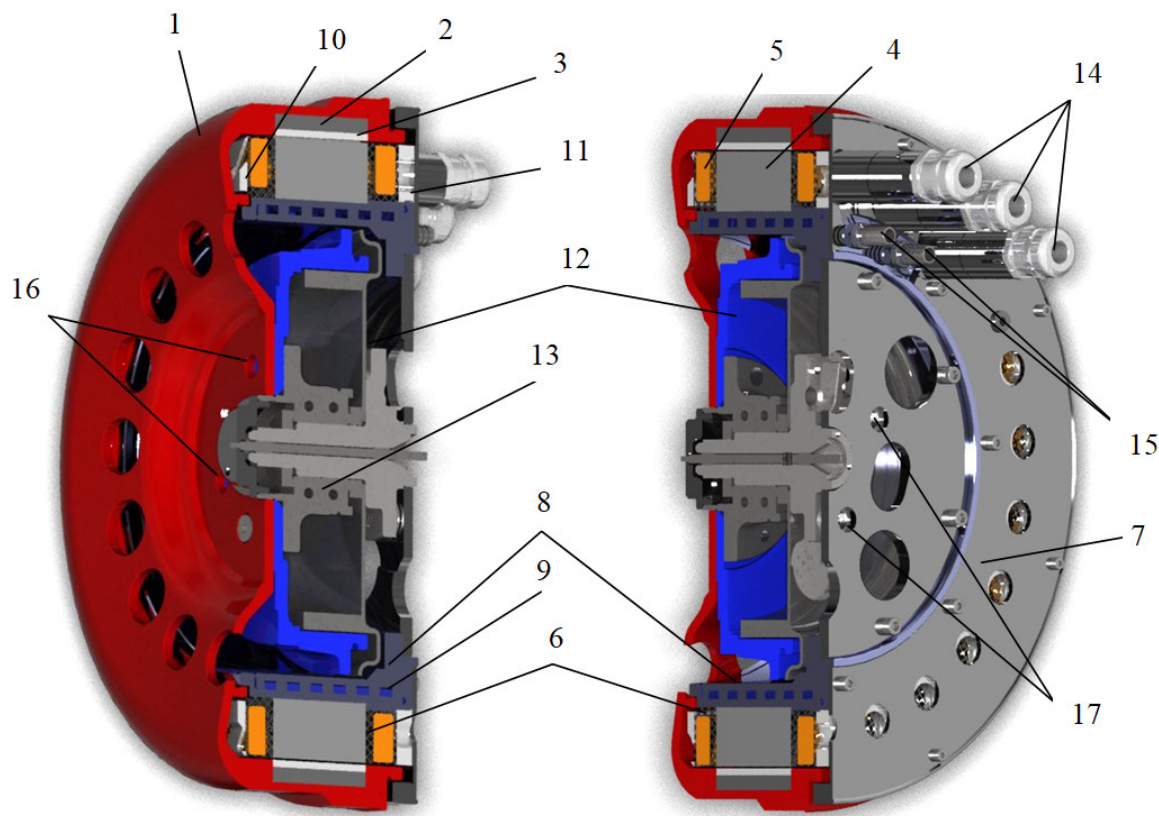


Figure 1. Models: The cross-section of the disassembled three-dimensional (3D) model of the SMzs200S32 motor, manufactured by Łukasiewicz Research Network—Upper Silesian Institute of Technology (Gliwice, Poland), and dedicated for assembly in the wheel hub of a car: 1—rotor, 2—rotor’s magnetic core, 3—magnet, 4—stator’s magnetic core, 5—stator winding coil ends, 6—resin, 7—permanent anchoring shield, 8—supporting structure, 9—casing with coolant ducts, 10—radiator of winding end, at drive end, 11—radiator of winding end, at non-drive side, 12—brake drum, 13—bearing assembly, 14—entry for supply wires, 15—cooling system ports, 16—rotor assembly openings, 17—stator assembly openings.

Figure 2 shows a model of the electromagnetic circuit of the motor, made in the ANSYS Motor CAD program. The computational model was calibrated with the results of laboratory tests, as presented in publications [54,55]. Calibration consisted of comparing the simulation results and measurements on the test stand. Sample results are presented later in the article (in Tables 1–5 and Figures 11–15).

Power losses in traction motors (especially those with high power and torque density) determine their efficiency, which affects not only the vehicle’s range and economy, but also the drive operating range and vehicle parameters such as maximum speed and driving dynamics.

In traction motors, the distribution of individual losses may vary depending on the operating condition of the motors. This may involve operation at high speeds and high power frequency. It may also include high temporary overload or low overload but for a long period of time. This is due to the current driving parameters of the car, which may be extremely different.

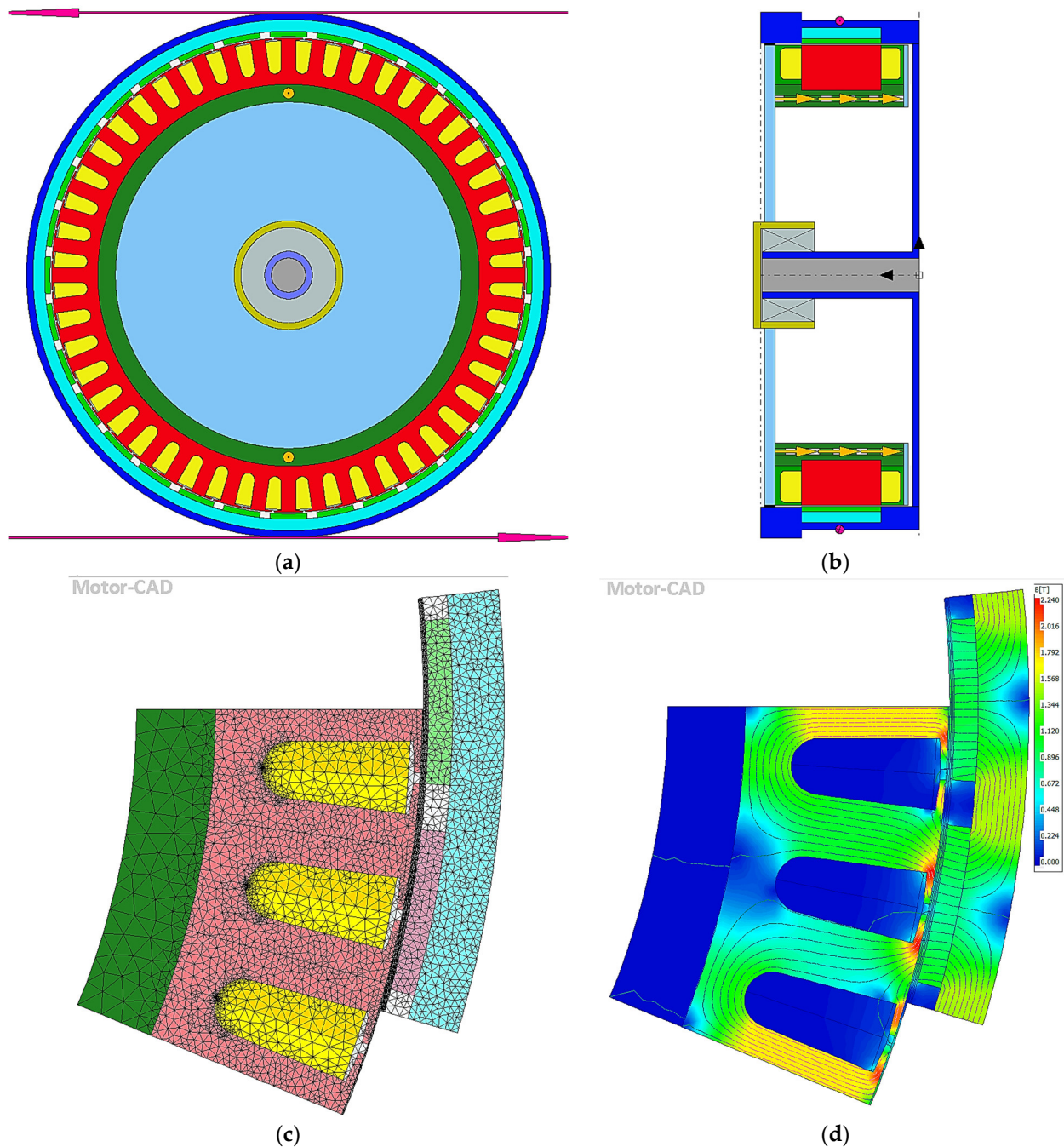


Figure 2. Electromagnetic circuit model of the motor in the ANSYS Motor CAD program. (a) model cross-section, (b) longitudinal section, (c) FEM mesh, (d) calculated distribution of induction from magnets.

2.1. Power Losses in the Motor Winding

Winding losses in the developed motor models were divided into permanent losses and so-called AC winding losses. The first ones are calculated based on the commonly known formula:

$$\Delta P = I^2 R(T),$$

where I is the RMS value of the supply current and $R(T)$ is the winding resistance as a function of temperature.

AC winding losses can be determined using two methods [56]:

(a) Full FEA.

(b) Hybrid FEA.

The full FEA method uses calculations on an accurate FEM model, taking into account induced eddy currents. In this method, losses are calculated separately in each conductor, which is very time-consuming. Because the analyses carried out in the work take into account calculations in a wide range of load and rotational speed, the hybrid FEA method was used for AC loss calculations.

The hybrid FEA method uses the distribution of magnetic induction in the slot determined using FEM to analytically calculate power losses, which are then multiplied by the selected correction factor. For the motor operating point corresponding to the maximum rotational speed and maximum load torque, power losses in the winding were calculated using both methods, and then the correction factor was determined from the formula:

$$k_{\text{Hybrid}}^{\text{Full}} = \frac{\Delta P_{\text{CuFull}}}{\Delta P_{\text{CuHybrid}}}$$

where ΔP_{CuFull} —winding losses related to the current displacement effect calculated using the full method; $\Delta P_{\text{CuHybrid}}$ —winding losses related to the current displacement effect calculated using the hybrid method.

2.2. Power Losses in the Motor's Magnetic Core

In the developed models, the Bertotti method [57–60] was used to calculate losses in the magnetic core of the motor, which allows hysteresis losses, losses caused by the flow of eddy currents and excess losses to be taken into account in the calculations. Total power losses in the motor core were determined by the formula:

$$\Delta P_{Fe}(t) = k_h B_m^2 f + \sigma \frac{b^2}{12} \left(\frac{dB}{dt}(t) \right)^2 + k_e \left(\frac{dB}{dt}(t) \right)^{\frac{3}{2}}$$

where k_h —the hysteresis coefficient; B_m —maximum value of magnetic induction; f —frequency of the supply voltage; σ —electrical conductivity of the core sheets; b —thickness of a single electrical sheet (without insulation); and k_e —excess loss factor.

Figure 3 shows the measured idle losses of the SMzs200S32 motor in generator and motor operation mode. The drive was powered by $U_{DC} = 350$ V, which is the rated voltage of the inverter selected for use in the drive.

In motor applications such as vehicle drives, the supply voltage from the inverter contains higher harmonics, which cause additional losses in the motor's magnetic core [61]. The research results presented in the literature [62] show that losses in the magnetic core of a motor powered by an inverter may be up to 45% higher. For this reason, the losses in the ferromagnetic core of the motor in the model were determined by subtracting from measured no-load loss (measured for motor work, with inverter and nominal voltage) the measured mechanical losses and the calculated no-load losses in the permanent magnets.

Figure 4 shows the dependence of core losses on the rotational speed when the motor is powered from an inverter with a voltage containing higher harmonics (determined using the previously described method) and calculated in the ANSYS Motor CAD program when powered with a sinusoidal voltage on the rotational speed. The calculated characteristic, presented in the figure below, was determined on the basis of multiplying the calculated no-load losses in the magnetic core by the coefficient resulting from the losses determined in the laboratory, so that the measured and calculated characteristics are as close as possible. Based on these characteristics, a coefficient (depending on the rotational speed) can be determined for a given type of inverter, which allows us, to some extent, to correct the losses in the motor core, calculated in the Motor CAD program, and to take into account the change caused by the higher harmonics of the supply voltage.

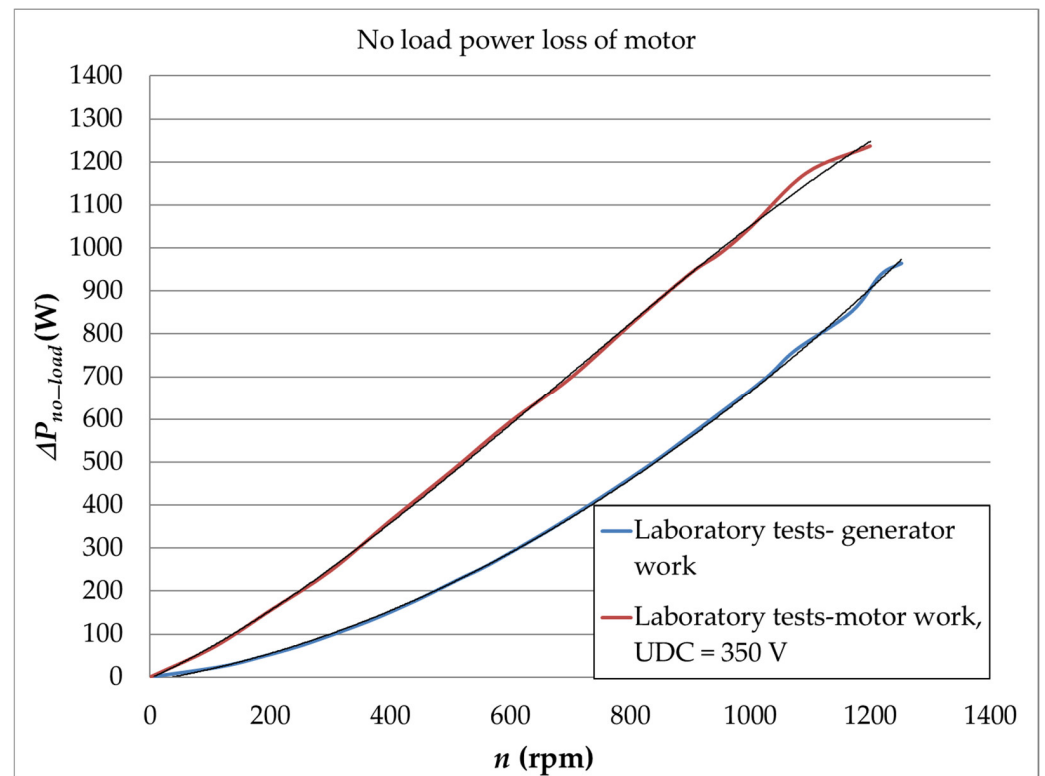


Figure 3. Laboratory determined no-load losses of the SMzs200S32 motor during generator operation and during motor operation and drive power supply with $U_{DC} = 350$ V.

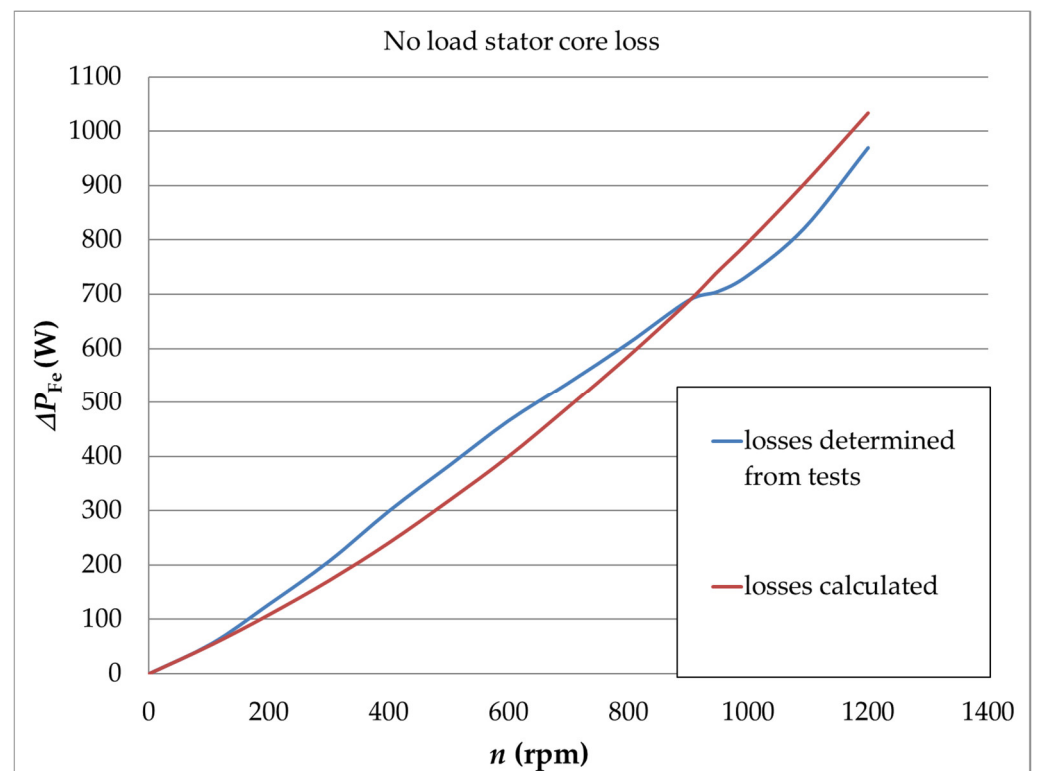


Figure 4. Determined power losses in the magnetic core of motor, based on the measured no-load characteristics and the characteristic calculated in the ANSYS Motor CAD program.

2.3. Mechanical Power Losses

The literature [63,64] provides empirical formulas for calculating total mechanical losses, giving approximate results that do not always take into account the type of bearings, the condition of the bearings and the actual ventilation system of the machine. In the case of non-standard structures, it is worth determining mechanical losses by measurement, especially since such measurement can be used to determine losses in the magnetic core of the stator.

Mechanical losses in the adopted motor design include the following:

- (a) Ventilation losses.
- (b) Bearing losses.

Ventilation losses result from air resistance, which, in the case of the motor with an external rotor, include losses related to air friction of the motor's movable disk and the rotor body.

Bearing losses result from friction in the bearing and depend on the bearing type and its condition. In the case of the motor in question, the motor structure is mounted on an original car bearing.

Mechanical losses were implemented in the computational model as a value dependent on the rotational speed. These losses were measured using a dynamometer on the motor without permanent magnets installed. Figure 5 shows the relationship between the measured mechanical losses and the rotational speed for the SMzs200S32 motor and calculated losses in the ANSYS Motor CAD program.

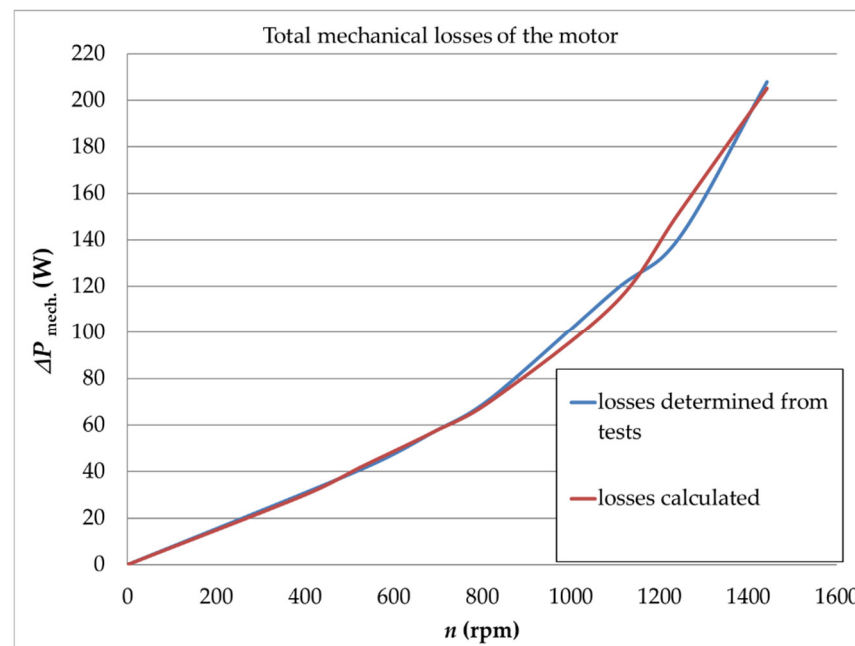


Figure 5. Mechanical losses of the SMzs200S32, measured in the laboratory and calculated in the simulation model.

2.4. Power Losses in Permanent Magnets

An important issue regarding power losses in traction motors with permanent magnets is the power loss generated in the permanent magnets. In the ideal case, when the magnetic field in the air gap contains only spatial harmonics synchronized with the rotor, no eddy currents flow in the magnets. In an electric motor with concentrated winding, the magnetic flux in the air gap, in addition to the fundamental harmonic, also contains subharmonics and higher harmonics, which cause eddy currents to be induced in the permanent magnets.

Literature analysis shows that there is no direct method for simple measurement of losses in permanent magnets. These losses can be estimated by calculation and esti-

mated by balancing the measured total power losses and the determined individual losses: mechanical losses, losses in the magnetic core and resistive losses [61].

The ANSYS Motor CAD program used in this work, using a two-dimensional field model of the motor, determines the induced eddy current density from the change in time of the potential of the magnetic vector A [56,65].

2.5. Thermal Model

The thermal model of the electric motor used to conduct the research work, was developed in the ANSYS Motor CAD program. The ANSYS Motor CAD program uses a cuboid winding model [56,66]. This approach allows for accurate representation of the three-dimensional heat transfer in all parts of the winding. The cuboid model, also known as the cuboid winding model, introduces the division of the winding into several cuboids. These three-dimensional volumes have different conductivities in each of the three dimensions (i.e., radially, tangentially and axially). This type of winding discretization allows for representation of heat transfer not only between different parts of the winding but also between different parts of the motor.

Figure 6 shows a thermal network for a synchronous motor excited by permanent magnets, with a single-bearing external rotor and a liquid cooling system in the supporting structure on which the stator is mounted.

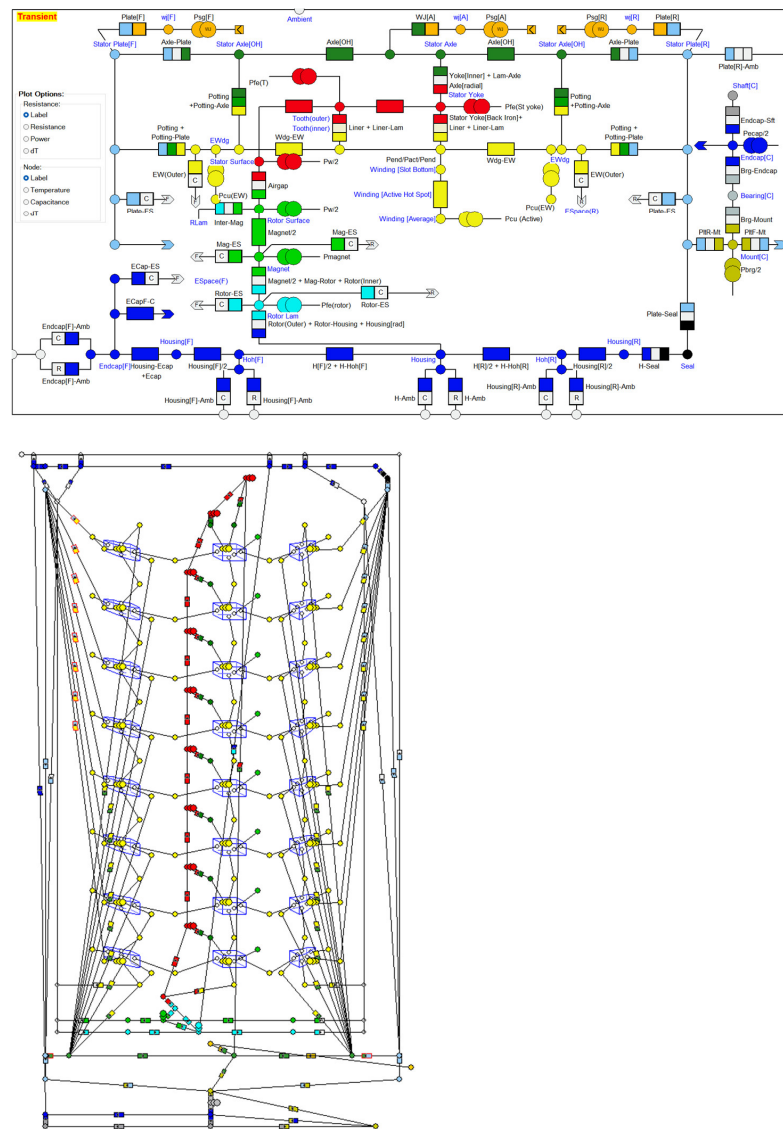


Figure 6. Thermal model of the motor in ANSYS Motor CAD.

The computational model consisting of the electromagnetic circuit and thermal model was calibrated based on the results of laboratory tests of the prototype motor. The SMzs200S32 prototype motor, manufactured by the Łukasiewicz Research network, Upper Silesian Institute of Technology, was equipped with a large number of temperature sensors. Small-sized Pt100 resistance sensors were placed not only in the winding end, which is standard, but also in other key components of the motor. The sensors were located in the stator winding and stator core on magnets in the rotor, on elements of the cooling system and on both sides of the motor (drive side (D) and non-drive side (ND)). The sensors were connected to a multi-channel recorder, enabling us to record temperature changes at individual measurement points. The sensor arrangement diagram is shown in Figure 7, a prototype of the motor is shown in Figure 8, and the sample sensors and their pinouts are shown in Figure 9.

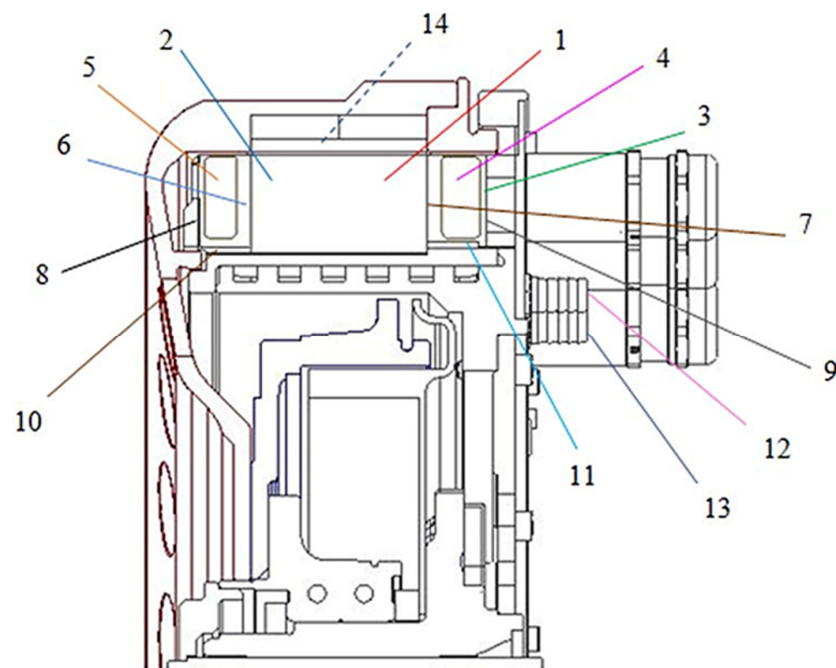


Figure 7. Cross-section of the SMzs200S32 prototype motor. Location of PT-100 temperature sensors in motor: 1—winding in slot, ND side, 2—winding in slot, D side, 3—zero point of the winding, 4—ND-side windings, 5—D-side windings, 6—D-side windings, 7—ND-side windings, 8—winding end D-side radiator, 9—winding end ND-side radiator, 10—D-side radiator element, 11—ND-side radiator element, 12—coolant inlet, 13—water outlet, 14—permanent magnets. ND—non-drive; D—drive.

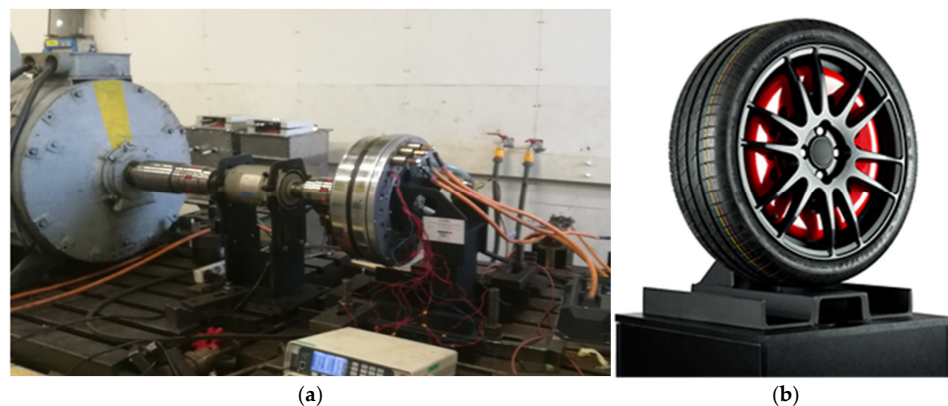


Figure 8. Prototype of SMzs200S32 motor: (a) in laboratory, (b) with wheel rim.



Figure 9. Arrangement of temperature sensors: (a) on the magnet, (b) in the slot (top of the slot), (c) temperature sensor terminals from the winding fronts, (d) temperature sensor terminals from the stator core (top of the tooth) and (e) stator core temperature sensor (bottom of the tooth/stator yoke).

In order to assess the accuracy of the thermal model, the calculation results of the ANSYS Motor CAD program were compared with the temperatures measured during laboratory tests. The temperatures of the top of the tooth, in the slot, in the winding fronts and of the side radiators were compared. Due to the impossibility of placing the sensors deep in the slot in the middle of the magnetic core (due to its large filling), temperature sensors were placed in the slot at a depth of several millimeters on each side of the motor, and their measurement was compared with the temperature of the straight part of the

winding face calculated in the model. The temperatures in these places of the winding should be very similar. The temperature sensor in the winding ends on the driving side was placed slightly lower than the temperature sensor on the side opposite to the driving side, which was also taken into account in the analysis. Figure 10 shows an example of the program calculation result with marked places where temperature sensors were placed in the real model. Tables 1–4 present exemplary comparisons of measured and calculated temperatures in the motor in a thermally steady state.

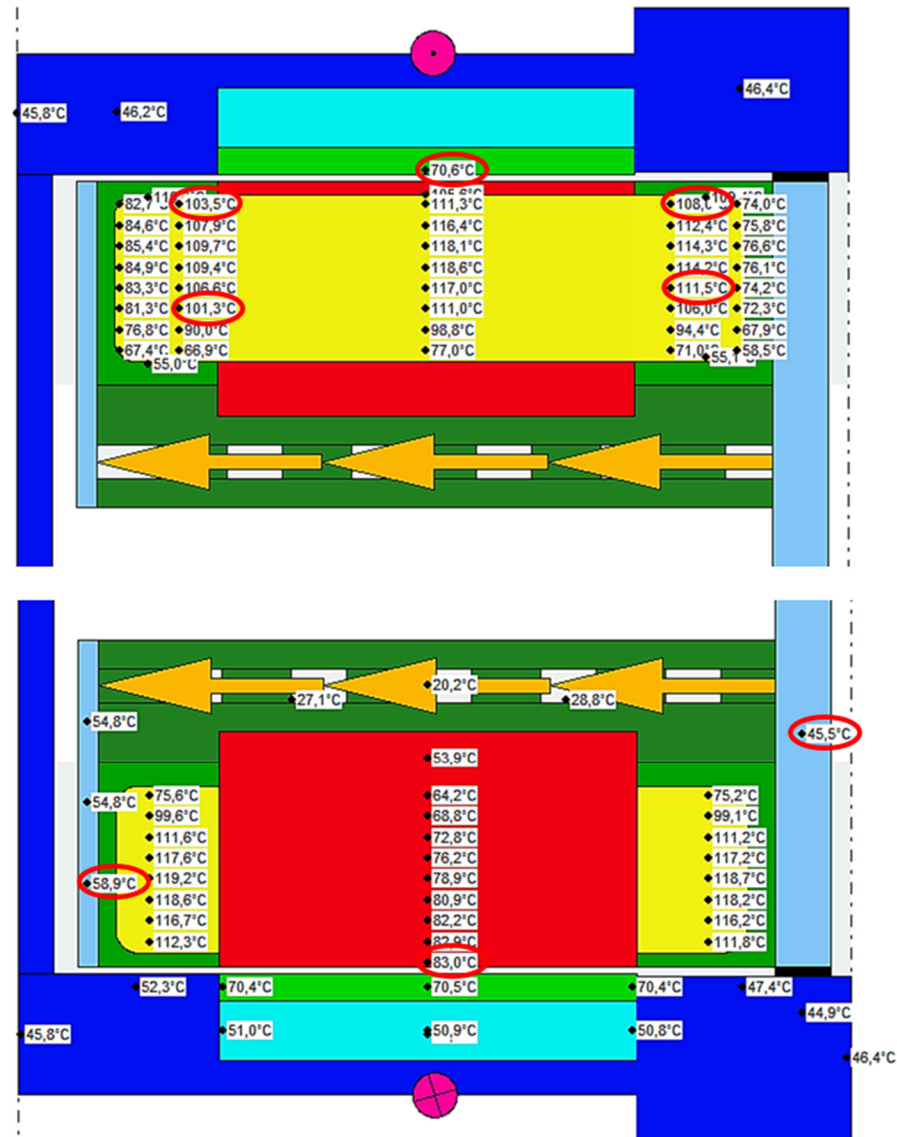


Figure 10. Calculated steady temperatures for the motor operating point: $T_m = 400 \text{ N}\cdot\text{m}$, $n = 950 \text{ rpm}$. ($V = 105 \text{ km/h}$), $T_{\text{ot}} = 18 \text{ }^\circ\text{C}$, coolant = $15.3 \text{ }^\circ\text{C}$, $q = 10 \text{ L/min}$.

Table 1. Comparison of the measured temperatures of individual motor components during the motor tests on the laboratory stand, with the temperatures calculated using the developed model in the ANSYS Motor CAD program: $T_m = 300 \text{ N}\cdot\text{m}$, $n = 950 \text{ rpm}$ ($V = 105 \text{ km/h}$), $T_{\text{ambient}} = 28.3 \text{ }^\circ\text{C}$, $T_{\text{Coolant}} = 23.8 \text{ }^\circ\text{C}$, $q = 10 \text{ L/min}$.

Component	Laboratory Tests	Calculation Model	ΔT [$^\circ\text{C}$]	ΔT [%]
Stator slot D	75	73.2	1.8	2.40
Stator slot ND	76.5	75.7	0.8	1.05
Winding end D	72.3	70.5	1.8	2.49
Winding end ND	76.8	76.1	0.7	0.91
Stator tooth D	65	64.4	0.6	0.92
Stator tooth ND	65.8	64.4	1.4	2.13
Magnets	67.1	64.9	2.2	3.28
Winding end radiator D side	49.5	49.1	0.4	0.81
Winding end radiator ND side	41.4	41.7	-0.3	-0.72

Table 2. Comparison of the measured temperatures of individual motor components during the motor tests on the laboratory stand, with the temperatures calculated using the developed model in the ANSYS Motor CAD program: $T_m = 350 \text{ N}\cdot\text{m}$, $n = 950 \text{ rpm}$. ($V = 105 \text{ km/h}$), $T_{\text{ambient}} = 28.8 \text{ }^\circ\text{C}$, $T_{\text{Coolant}} = 24.1 \text{ }^\circ\text{C}$, $q = 10 \text{ L/min}$.

Component	Laboratory Tests	Calculation Model	ΔT [$^\circ\text{C}$]	ΔT [%]
Stator slot D	92.3	91.2	1.1	1.19
Stator slot ND	94	94.6	-0.6	-0.64
Winding end D	88.9	88.7	0.2	0.22
Winding end ND	95.8	96.4	-0.6	-0.63
Stator tooth D	78.7	77	1.7	2.16
Stator tooth ND	77.5	77	0.5	0.65
Magnets	72.1	72	0.1	0.14
Winding end radiator D side	57.5	57.8	-0.3	-0.52
Winding end radiator ND side	47.5	47.6	-0.1	-0.21

Table 3. Comparison of the measured temperatures of individual motor components during the motor tests on the laboratory stand, with the temperatures calculated using the developed model in the ANSYS Motor CAD program: $T_m = 400 \text{ N}\cdot\text{m}$, $n = 950 \text{ rpm}$. ($V = 105 \text{ km/h}$), $T_{\text{ambient}} = 18 \text{ }^\circ\text{C}$, $T_{\text{Coolant}} = 23.8 \text{ }^\circ\text{C}$, $q = 10 \text{ L/min}$.

Component	Laboratory Tests	Calculation Model	ΔT [$^\circ\text{C}$]	ΔT [%]
Stator slot D	103.5	103.5	0	0.00
Stator slot ND	105.6	108	-2.4	-2.27
Winding end D	99.3	101.3	-2	-2.01
Winding end ND	108	111.5	-3.5	-3.24
Stator tooth D	85.7	83	2.7	3.15
Stator tooth ND	83.9	83	0.9	1.07
Magnets	70.8	70.5	0.3	0.42
Winding end radiator D side	60	58.9	1.1	1.83
Winding end radiator ND side	45.9	45.5	0.4	0.87

Table 4. Comparison of the measured temperatures of individual motor components during the motor tests on the laboratory stand, with the temperatures calculated using the developed model in the ANSYS Motor CAD program: $T_m = 315 \text{ N}\cdot\text{m}$, $n = 1360 \text{ rpm}$. ($V = 150 \text{ km/h}$), $T_{\text{ambient}} = 24 \text{ }^\circ\text{C}$, $T_{\text{Coolant}} = 19 \text{ }^\circ\text{C}$, $q = 10 \text{ L/min}$.

Component	Laboratory Tests	Calculation Model	ΔT [$^\circ\text{C}$]	ΔT [%]
Stator slot D	104	107.2	−3.2	−3.08
Stator slot ND	105.6	111.5	−5.9	−5.59
Winding end D	103.2	103.9	−0.7	−0.68
Winding end ND	108.3	113.6	−5.3	−4.89
Stator tooth D	85	86.6	−1.6	−1.88
Stator tooth ND	82.9	86.6	−3.7	−4.46
Magnets	76.5	73	3.5	4.58
Winding end radiator D side	59.9	61.5	−1.6	−2.67
Winding end radiator ND side	49.1	49.6	−0.5	−1.02

Figures 11–15 present both the temperature courses of motor components calculated by the program and measured during the heating tests for the selected point of work: $n = 950 \text{ rpm}$ and $T_m = 400 \text{ N}\cdot\text{m}$.

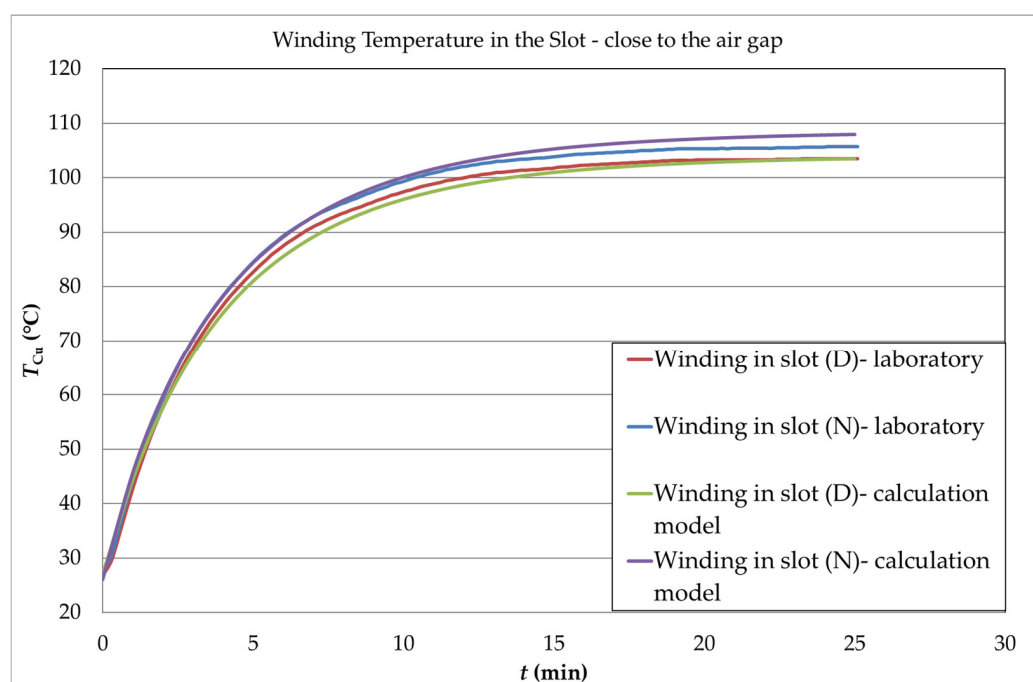


Figure 11. Comparison of calculated winding temperatures in the slot with measured temperatures at the test stand. $T_m = 400 \text{ N}\cdot\text{m}$, $n = 950 \text{ rpm}$. ($V = 105 \text{ km/h}$), $T_{\text{ambient}} = 18 \text{ }^\circ\text{C}$, $T_{\text{Coolant}} = 15.3 \text{ }^\circ\text{C}$, $q = 10 \text{ L/min}$.

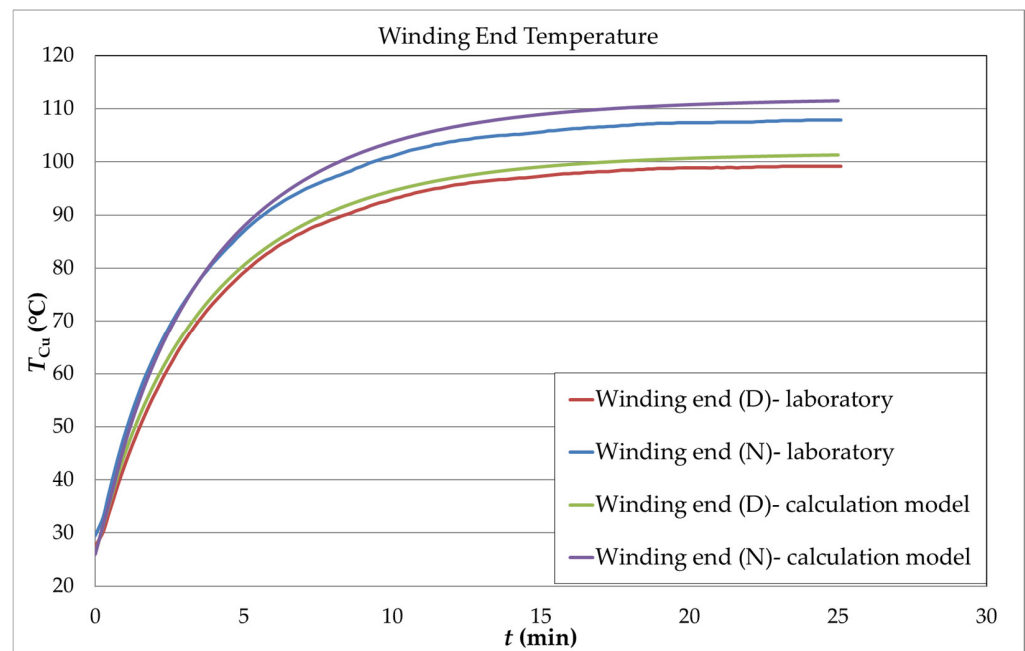


Figure 12. Comparison of calculated winding end temperatures in the slot with measured temperatures at the test stand. $T_m = 400 \text{ N}\cdot\text{m}$, $n = 950 \text{ rpm}$. ($V = 105 \text{ km/h}$), $T_{\text{ambient}} = 18 \text{ }^\circ\text{C}$, $T_{\text{Coolant}} = 15.3 \text{ }^\circ\text{C}$, $q = 10 \text{ L/min}$.

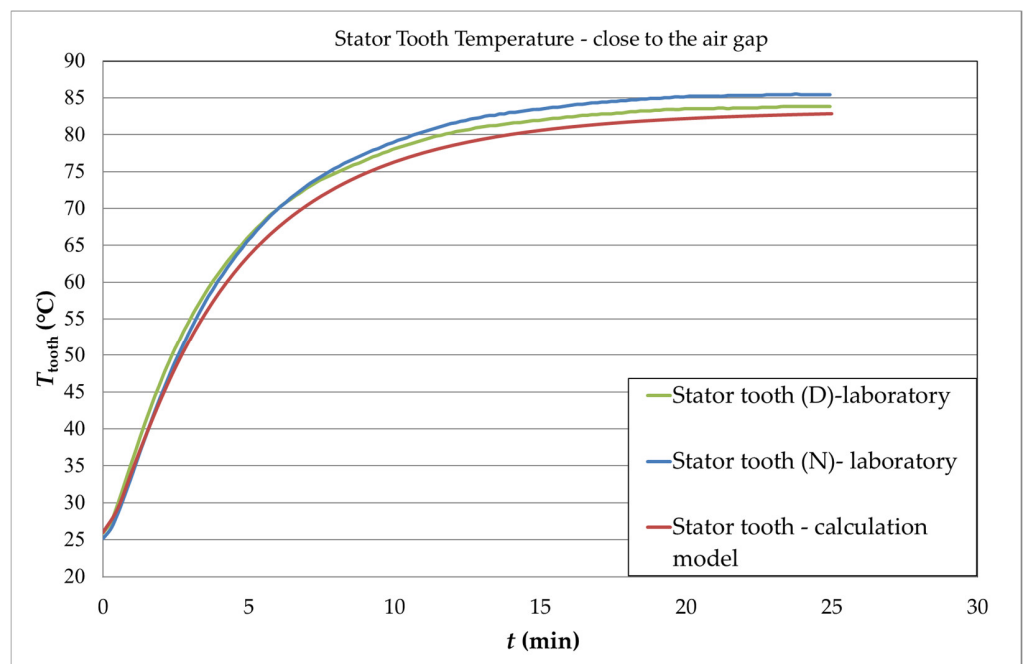


Figure 13. Comparison of calculated stator tooth temperatures in the slot with measured temperatures at the test stand. $T_m = 400 \text{ N}\cdot\text{m}$, $n = 950 \text{ rpm}$. ($V = 105 \text{ km/h}$), $T_{\text{ambient}} = 18 \text{ }^\circ\text{C}$, $T_{\text{Coolant}} = 15.3 \text{ }^\circ\text{C}$, $q = 10 \text{ L/min}$.

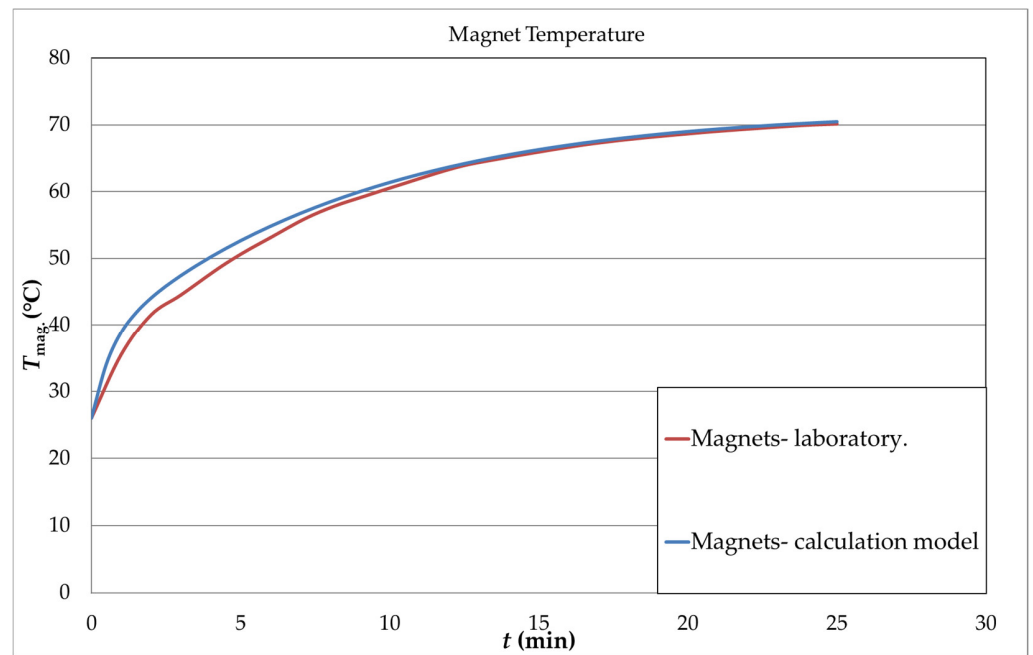


Figure 14. Comparison of calculated magnet temperatures in the slot with measured temperatures at the test stand. $T_m = 400$ N m, $n = 950$ rpm. ($V = 105$ km/h), $T_{ambient} = 18$ °C, $T_{Coolant} = 15.3$ °C, $q = 10$ L/min.

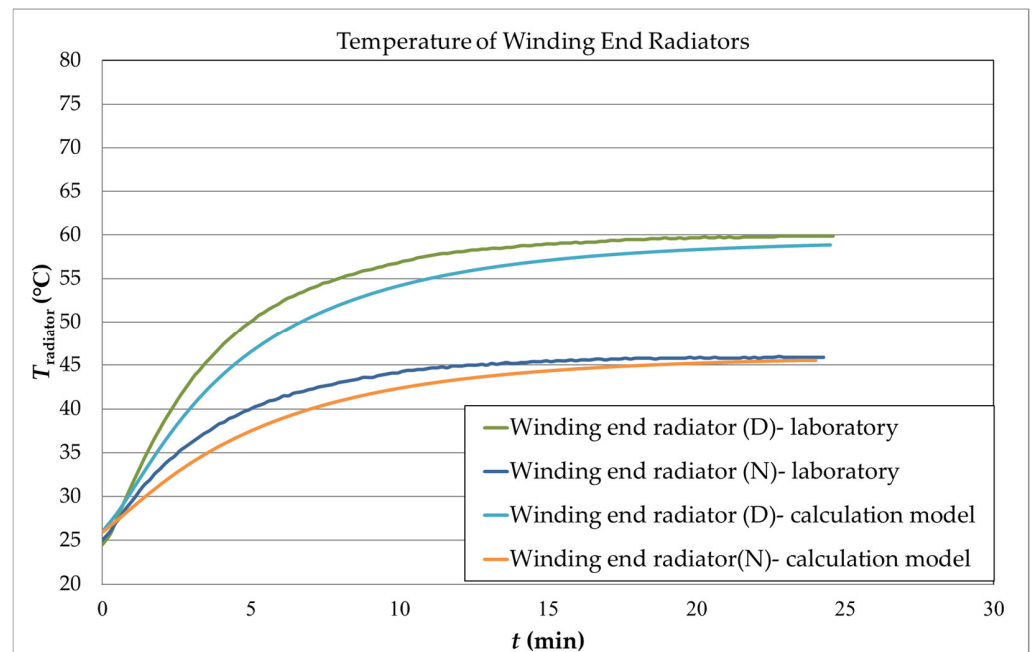


Figure 15. Comparison of calculated winding end radiator temperatures in the slot with measured temperatures at the test stand. $T_m = 400$ N m, $n = 950$ rpm. ($V = 105$ km/h), $T_{ambient} = 18$ °C, $T_{Coolant} = 15.3$ °C, $q = 10$ L/min.

Comparing the results of heating tests in the laboratory with the calculation results of the ANSYS Motor CAD program allows us to determine whether the computational model reflects the actual thermal states of the motor. The comparison included not only steady states but also transient states because the model was to be used to simulate motor operation during car driving cycles.

The discrepancy between the program calculation results and the laboratory test results for the main elements of the electromagnetic circuit (such as the stator winding, magnetic core or permanent magnets) in the places of temperature measurement does not exceed $\Delta T = 6$ K, which is a difference of several percent.

3. Driving Cycles

The Lab module of the ANSYS Motor CAD program was used to conduct thermal analysis of the motor while the car was driving. It allows simulations to be performed on a coupled electromagnetic–thermal model of the motor. In electric motor tests, various cycles can be assigned using a model created for a selected type of car. Based on the vehicle speed course in the driving cycle under consideration, the program calculates the torque demand. Calculations can be performed taking into account the coupling of the electromagnetic field with the temperature field. Such calculations take into account the effect of temperature on the operating parameters of the electromagnetic circuit.

The vehicle model is based on the analysis of forces acting on the vehicle while driving at a constant speed and during acceleration and braking. The individual formulas for the forces occurring in the vehicle model are as follows [56]:

$$F_R = k_r \cdot m \cdot g \cdot \cos\theta,$$

where F_R —force caused by rolling resistance; k_r —rolling resistance coefficient; m —vehicle mass; g —gravitational acceleration; and θ —slope of the hill.

$$F_D = \frac{1}{2}\rho(V + V_0)^2 C_d A_f,$$

where F_D —force caused by aerodynamic drag; ρ —air density; V —vehicle speed; V_0 —headwind speed; C_d —vehicle air drag coefficient; and A_f —vehicle frontal area.

$$F_c = m \cdot g \cdot \sin\theta,$$

where F_C —climbing force.

$$F_T = mg(k_r \cos\theta + \sin\theta) + \frac{1}{2}\rho(V + V_0)^2 C_d A_f,$$

where F_T —total force required to keep the vehicle moving continuously.

$$F_a = m \cdot a \cdot \delta,$$

where F_a —dynamic force caused by vehicle acceleration; δ —mass correction factor.

$$T_{motor} = \frac{(F_a + F_T) \cdot r_w}{n_d}$$

where T_{motor} —motor torque; r_w —wheel radius; and n_d —final drive ratio.

The driving cycles are described as a set of points on the speed curve determined during tests on real vehicles.

The Artemis transient cycles [67–69] were used to conduct the thermal analysis of the motor:

- (a) Artemis Urban;
- (b) Artemis Road;
- (c) Motorway150;
- (d) US06.

Table 5 presents the parameters of the considered driving cycles, while Table 6 presents the parameters adopted for the car model.

Table 5. Parameters of the driving cycles considered.

Parameter	Artemis Urban	Motorway 150	US06
Driving time (s)	993	1068	596
Distance on the road (km)	4.874	29.547	12.89
Average vehicle speed (km/h)	17.7	99.6	77.84
Maximum vehicle speed (km/h)	57.3	150.4	129
Percentage of speed range in cycle (%)			
Stop ($V = 0$ km/h)	21	1	6.7
Low speed ($0 < V \leq 50$ km/h)	77	14	23
Average speed ($50 < V \leq 90$ km/h)	2	14	13.3
High speed ($V > 90$ km/h)	0	71	57

Table 6. The parameters of various car models used for calculations.

Parameter	Nissan Leaf
Vehicle weight (kg)	1820
Vehicle frontal area (m ²)	2.3
Circle radius (m)	0.3
Vehicle rolling resistance coefficient	0.007
Vehicle drag coefficient	0.28
Mass correction factor	1.04
Air density (kg/m ³)	1.225
Mechanical transmission	1
Share of electric motor in driving torque	0.5
Electric motor share in braking torque	0.25

On this basis, the required torque curves for individual driving cycles were calculated. Figure 16 shows the required torque curves and vehicle speed curves.

The first cycle analyzed was the Artemis Urban cycle. The courses show that the highest torque is required after about 200 s during vehicle start-up and after about 350 s during braking. In the course of the required torque for the Artemis Motorway 150 cycle, it can be seen that the highest torques are required at lower speeds, during simulated motorway access (up to about $V = 70$ km/h), while at higher vehicle speeds, the required torque is lower. The last cycle considered is the dynamic cycle characterized by the highest torque requirements among the cycles considered, visible at the beginning of the cycle, when driving at increased speed and during dynamic maneuvers at the end of the cycle.

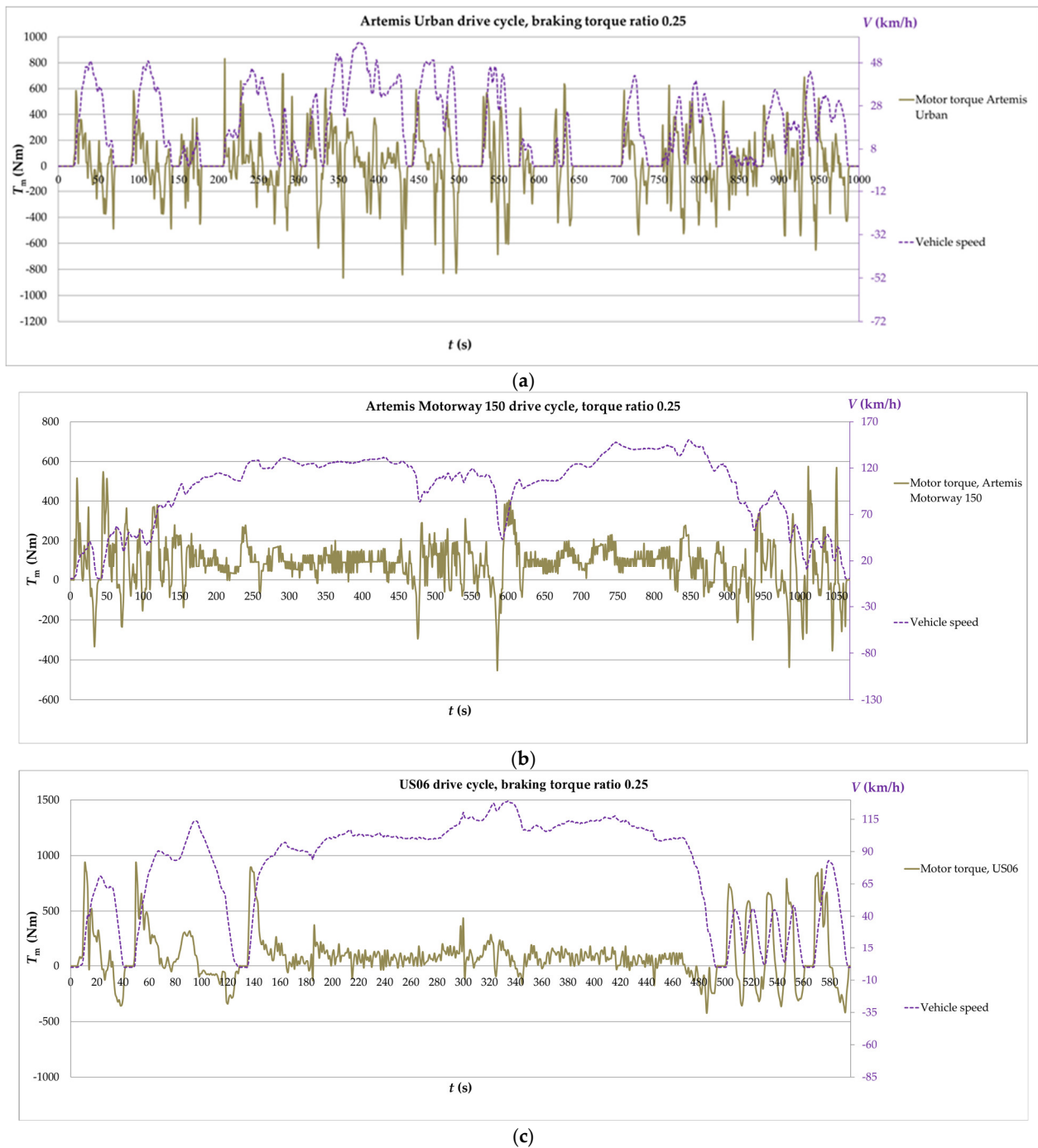


Figure 16. Calculated course of the required motor torque in a Nissan Leaf vehicle with dual-wheel drive, running in the driving cycle: (a) Artemis Urban, (b) Artemis Motorway 150, (c) US06 (motor share factor in braking torque 0.25).

4. Changing the Length of the Motor's Magnetic Core

The design change of reducing the length of a motor intended for installation in the wheel hub may result from the desire/necessity to reduce the mass of the motor or from the need to adapt its axial dimension to the position of the suspension system elements or brake system elements such as brake disks. Reducing the length of the magnetic core reduces the generated torque of the motor. The aim of this analysis was to compare the operation of motors meeting the requirements of the driving cycles under consideration. For this reason, the number of turns had to be increased to meet the requirements of the US06 driving cycle

in the following chapters. The number of turns and the length of the magnetic core were selected so that the maximum torque was as close as possible in the compared motors and met the demand for the maximum torque of all the driving cycles under consideration. The selection of the length and number of turns due to the dependence of the maximum torque on saturations must be carried out to some extent by trial and error.

Calculations were performed for three different lengths of the magnetic core of the motor:

(a) $L_{Fe} = 60$ mm.

(b) $L_{Fe} = 50$ mm.

(c) $L_{Fe} = 45$ mm.

Table 7 presents selected parameters of the electromagnetic circuit with different magnetic core lengths.

Table 7. Parameters of the electromagnetic circuit.

Parameter	$L_{Fe} = 60$ mm	$L_{Fe} = 50$ mm	$L_{Fe} = 45$ mm	Unit
Stator core	9.5	8	7.2	kg
Winding	4.5	4	3.8	kg
Rotor core	4.4	3.7	3.3	kg
Magnets	1.6	1.4	1.2	kg
Weight of the electromagnetic circuit	20	17.1	15.5	kg
Number of parallel wires	31	22	17	-
Filling the stator slot	0.7022	0.7067	0.69	-
Number of turns/phase	80	112	144	-
Winding wire diameter	0.65 copper 0.729 with insulation	0.65 copper 0.729 with insulation	0.65 copper 0.729 with insulation	-

Figure 17 shows the maximum torque characteristics of the three motors under consideration. The course of the characteristics can be divided into zones according to the motor control method. The first control zone covers the motor operation range with constant torque. The second control zone covers the motor operation range in which the motor is de-excited.

The characteristic operating point of the motor, with given power supply parameters (with given supply voltage and supply current), is the so-called base point, which is the operating point with constant torque at the highest rotational speed. The base point moves to increasingly lower rotational speeds with the reduction in the magnetic core length. For comparison, the motor with the longest package has a maximum torque up to a car speed of approx. $V = 110$ km/h, while the motor with the shortest package has the same maximum torque up to a car speed of $V = 60$ km/h.

Additionally, Figure 5 shows the dependencies of the maximum motor torques on the rotational speed, which are required for the modeled vehicle driving cycles: Artemis Urban, Artemis Motorway 150 and US06. It is worth noting that the Artemis Urban driving cycle is within the rotational speed range in the first control zone of all three motors.

As expected, the most demanding drive cycle in terms of the torque demand generated by the motor is the US06 cycle, which is characterized by the highest torque requirement in both the first and second control zones.

Shortening the magnetic core results in a reduction in the mass of the electromagnetic circuit but also limits the range of the motor in the second control zone. The mass of the electromagnetic circuit of a motor with a core length of $L_{Fe} = 45$ mm is approximately 15.5 kg and of a motor with a core length of $L_{Fe} = 50$ mm is approximately 17 kg, while for the motor with a core length of $L_{Fe} = 60$ mm and $2p = 32$, for which the prototype was made, $m = 20$ kg.

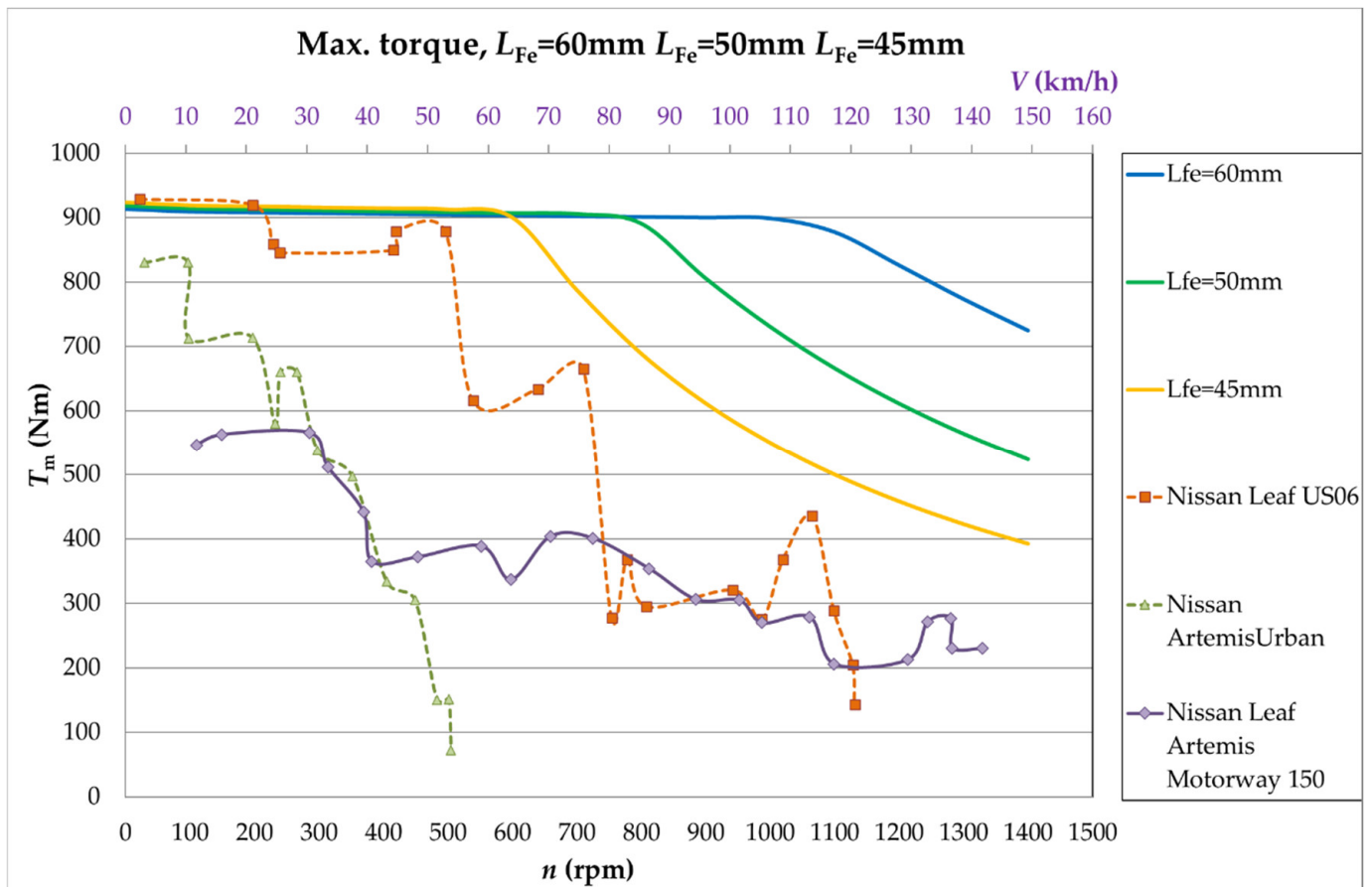


Figure 17. Calculated characteristics of maximum motor torques for different magnetic core lengths with plotted maximum torques occurring for the considered Nissan Leaf car model for the Artemis Urban, Artemis Motorway 150 and US06 driving cycles.

4.1. Changing the Length of the Motor's Magnetic Core—Artemis Urban Driving Cycle

Figure 18a shows the temperature curves in the motor for a cycle repeated five times. As expected, the winding temperature reaches the highest values for the motor with the shortest package. The maximum temperature for the motor with the shortest package was $T_{Cu} = 108\text{ }^{\circ}\text{C}$ in the last repetition of the cycle and was approximately $\Delta T_{Cu} = 26\text{ }^{\circ}\text{C}$ higher than the temperature of the motor with the longest package. The achieved operating temperatures of the motor winding are relatively low in relation to the permissible temperature of the slot insulation, winding wire and epoxy resin. Similarly, the operating temperatures of the permanent magnets in all the motors did not exceed the value of $T_{mag.} = 65\text{ }^{\circ}\text{C}$, which is a safe temperature, especially in the absence of de-excitation. The temperature difference in the magnets of the motor with the longest and shortest package does not exceed $\Delta T_{mag.} = 4\text{ }^{\circ}\text{C}$. Similarly, the temperature difference in the stator magnetic core between motors with extremely different core lengths in the tooth at the air gap is approximately $\Delta T_{tooth} = 10\text{ }^{\circ}\text{C}$ and in the yoke approximately $\Delta T_{yoke} = 5\text{ }^{\circ}\text{C}$.

Figure 19 shows the calculated power loss curves in the winding, in the permanent magnets and in the stator magnetic core. Figure 19a–c compare the calculation results for three magnetic core lengths. The power losses in the winding increase with decreasing core length, as expected, and the temperature difference between the motor models increases with the current intensity. The losses in the magnets and in the magnetic core decrease with decreasing magnetic core length.

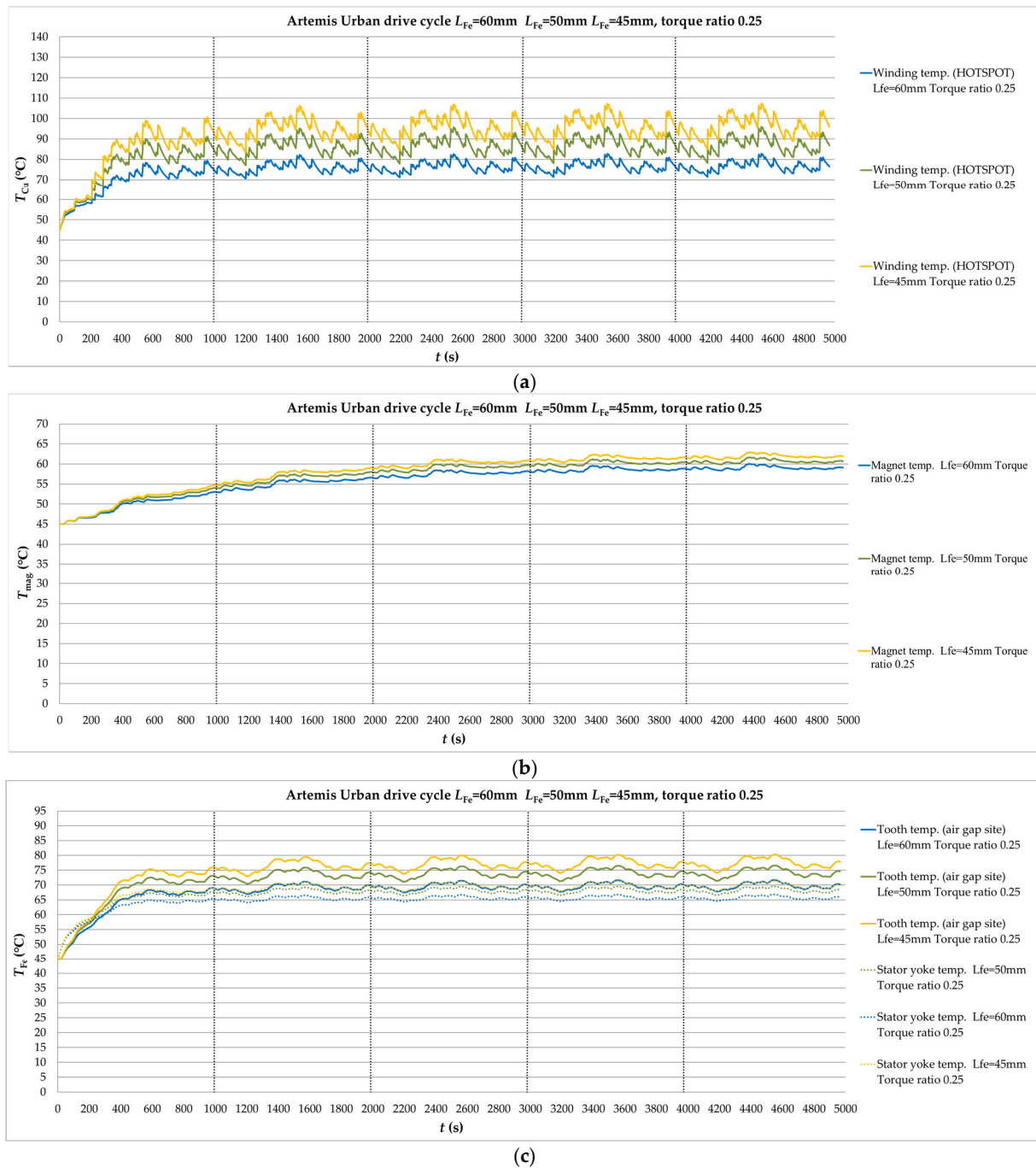


Figure 18. Calculated temperature profile of individual motor components (for three core lengths) in the considered Nissan Leaf car with dual-motor drive, running in the Artemis Urban driving cycle repeated 5 times (braking torque participation factor 0.25): (a) maximum winding temperature, (b) magnet temperature, (c) stator magnetic core temperature.

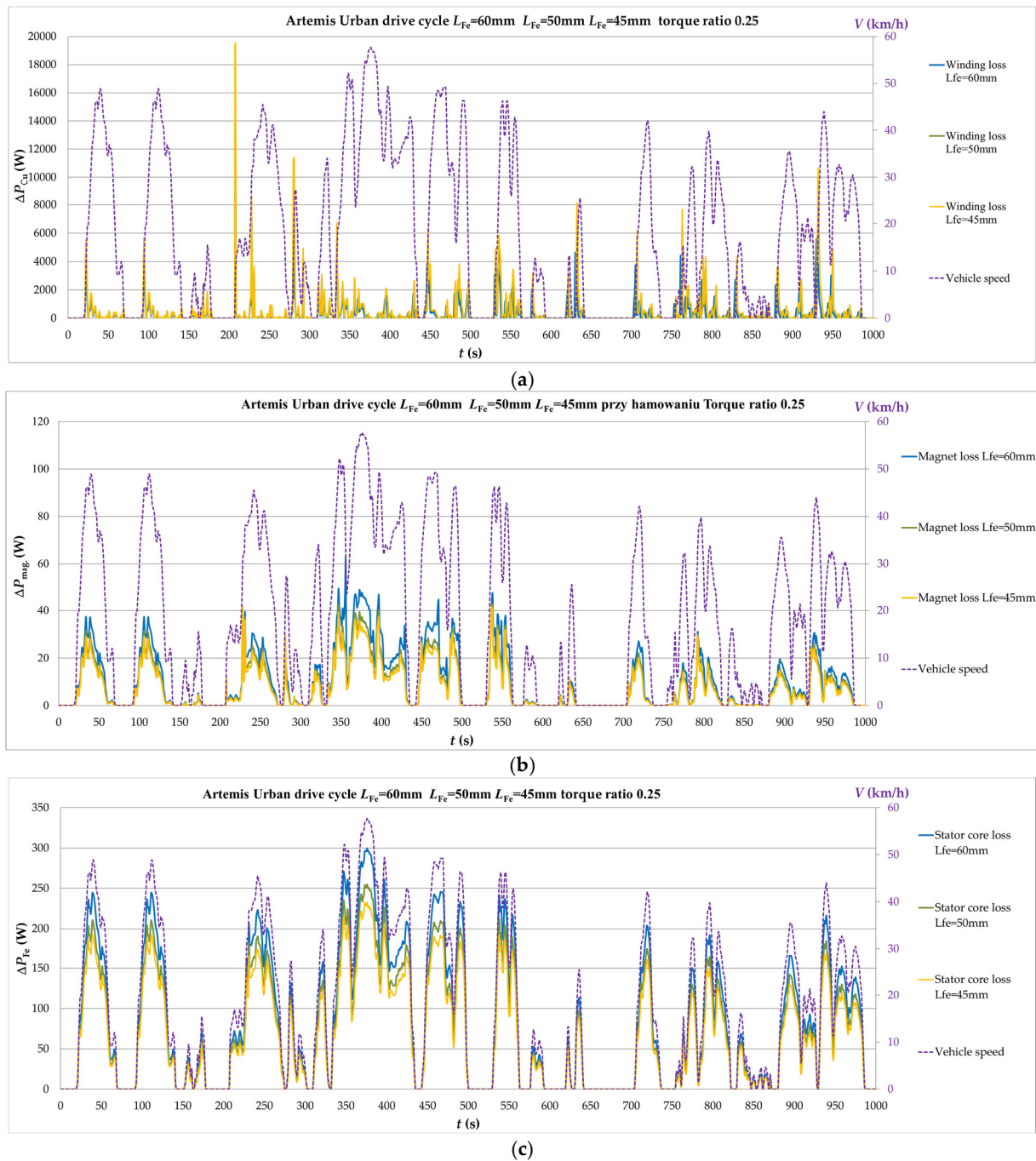
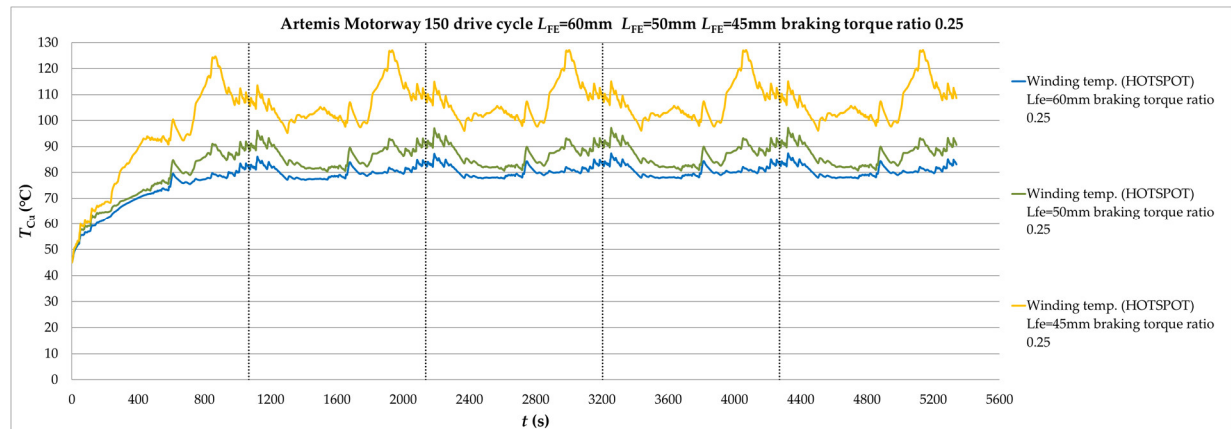


Figure 19. Calculated course of motor power losses (for three core lengths) in the considered Nissan Leaf car with dual-motor in-wheel drive, moving in the Artemis Urban driving cycle: (a) in the winding, (b) in the magnets, (c) in the stator magnetic core.

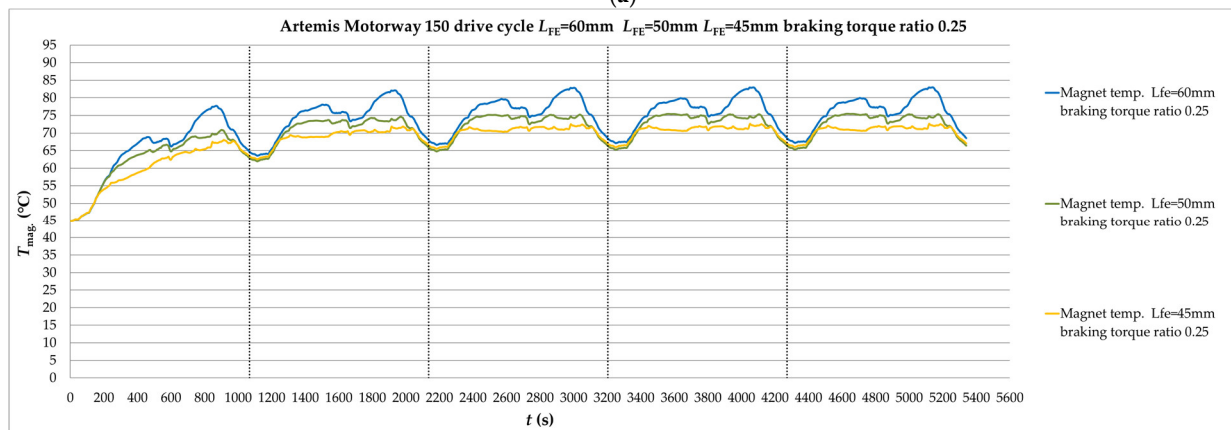
4.2. Changing the Length of the Magnetic Core of the Motor—Artemis Motorway 150 Driving Cycle

The next analyzed driving cycle is the Artemis Motorway 150 cycle. The cycle involves driving the car at a speed higher than the city driving range, forcing the motor to work in the second control zone. In this range, the motors operate in different power supply conditions. The shorter the magnetic core package, the more the motor must work with field weakening. As a result, the motor must be supplied with a higher current to obtain the required torque. Figure 8 presents, analogously to the analysis of the Artemis Urban cycle, the temperature curves of the winding, permanent magnets and magnetic core. Figure 20a,

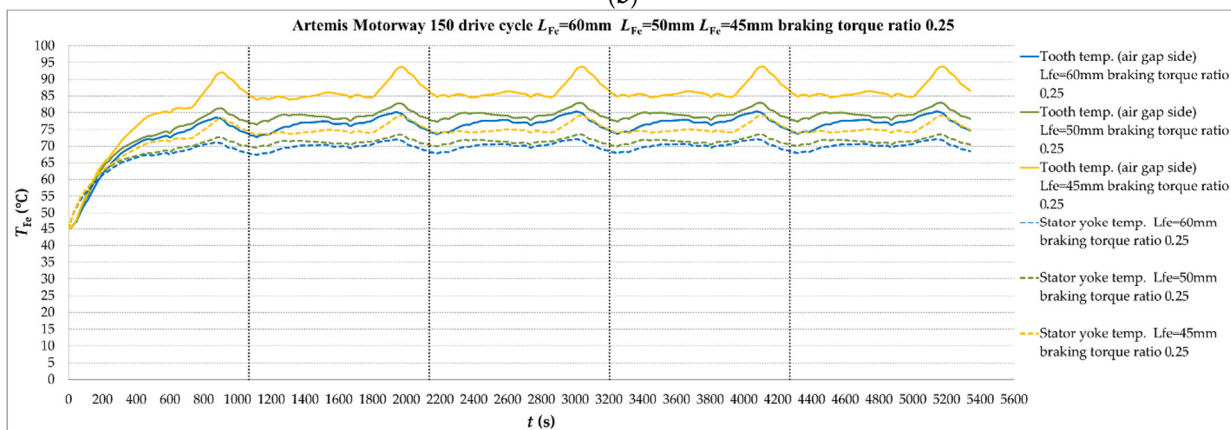
showing the winding temperature curve, shows how from about the 150th second of the cycle, when the car begins to increase speed above $V = 70$ km/h, the temperature of the motor with the shortest package begins to increase significantly in relation to the other two motors. This is due to the need for earlier field weakening in relation to the other two motors.



(a)



(b)



(c)

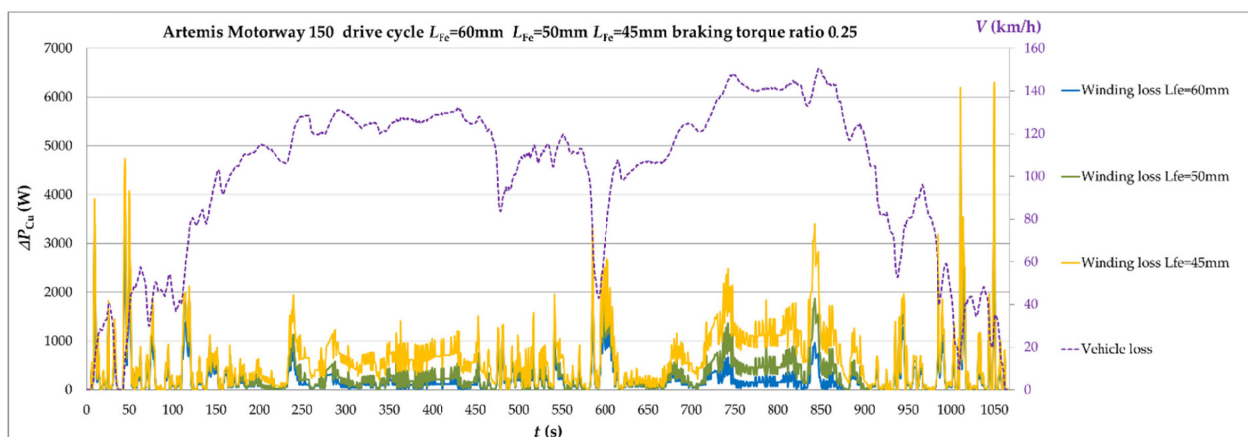
Figure 20. Calculated course of temperatures of individual motor components in the considered Nissan Leaf car with dual-motor drive in the Artemis Motorway 150 driving cycle repeated 5 times (motor participation factor in braking moment 0.25). Courses for three lengths of magnetic cores: (a) maximum winding temperature, (b) magnet temperature, (c) stator magnetic core temperature.

The temperature of the motor with the $L_{Fe} = 50$ mm package also begins to increase significantly in relation to the motor with the $L_{Fe} = 60$ mm package, but only from about

700 s, when the vehicle speed increases above $V = 120$ km/h. At this time, the motor with the $L_{Fe} = 50$ mm magnetic core package is already operating with relatively large de-excitation. The motor with the $L_{Fe} = 60$ mm package is on the verge of starting to work in the second control zone, while the motor with the $L_{Fe} = 45$ mm package is de-excited very strongly.

The compared motor winding temperature curves reflect the process of significant temperature increase during de-excitation very well. At $t = 864$ s, the winding temperature of the motor with the shortest core reaches a maximum value of approx. $T_{Cu} = 125$ °C. The winding temperature of the motor with the medium-length package reaches a value of approx. $T_{Cu} = 90$ °C at this time. This is a local extreme of the curve, and the corresponding maximum temperature is comparable to the temperatures reached at the end of the cycle, where there is an exit from the motorway and a series of braking and accelerations with higher torques, at lower speeds, not including the second motor control zone. The motor with the longest package reaches higher winding temperatures in other ranges of the work cycle, where higher torques are required. Control using field weakening has a beneficial effect on the temperature of permanent magnets, which is visible in the course of the magnet temperature in Figure 20. In contrast to the winding temperature, the lowest magnet temperatures are achieved by the motor with the shortest package. The courses also show the influence of the motor speed on the temperature course. The motor with the shortest package, after starting work in the second control zone, is characterized by a small temperature variability around the level of approx. $T_{mag} = 70$ °C from the second repetition of the driving cycle. The course of the magnet temperature of the motor with the longest package shows a greater dependence of the temperature on the increase in vehicle speed. This is also supported by the calculated power losses generated in permanent magnets, shown in Figure 21. Power losses generated in magnets, which have a direct effect on their operating temperature, for a motor with a package length of $L_{Fe} = 60$ mm, visibly increase with the vehicle speed. In turn, the power losses in the magnets of the shortest motor decrease after the vehicle speed exceeds approx. $V = 60$ km/h, and then increase with decreasing vehicle speed.

In the motor with the $L_{Fe} = 50$ mm package, when the vehicle speed exceeds approx. $V = 90$ km/h, the magnet losses are maintained at a practically constant level, while when the vehicle speed exceeds approx. $V = 140$ km/h, the magnet losses decrease with the vehicle acceleration. A similar relationship applies to the power losses in the magnetic core (Figure 21c), which are also limited in the second control zone. On the other hand, the stator magnetic core temperature is more dependent on the winding temperature; therefore, despite field weakening, the core temperature increases with the shortening of the magnetic core.



(a)

Figure 21. Cont.

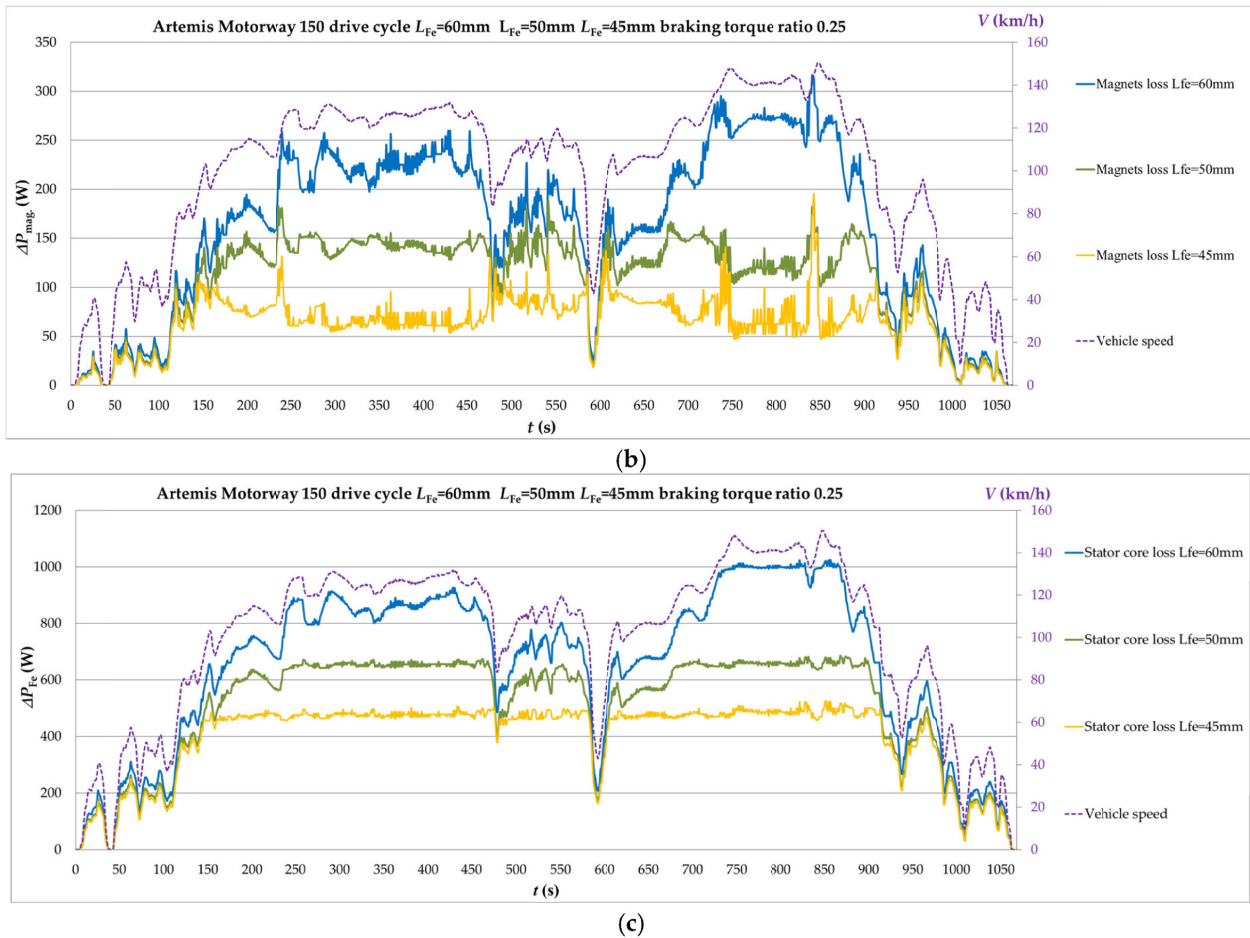


Figure 21. Calculated course of motor power losses in the considered Nissan Leaf car with dual-motor drive in the Artemis Motorway 150 driving cycle: (a) in the winding, (b) in the magnets, (c) in the stator magnetic core.

4.3. Change in the Length of the Magnetic Core of the Motor—US06 Driving Cycle

The last driving cycle considered is the US06 cycle, which reflects the dynamic driving of the car at low speeds and when driving at a higher speed. Figure 22a presents the calculated courses of maximum temperatures of the motor winding. Due to significant differences between the winding temperatures of motors with different package lengths, additional driving simulations were performed, taking into account different coefficients of the motor's participation in the car's braking. Simulations were performed for the braking participation coefficient equal to 0.25, 0.1 and 0.35 for the motor with the longest magnetic core package.

The analysis showed that the motor with the shortest package, after the first repetition of the driving cycle, reaches very high winding temperatures equal to $T_{Cu} = 195\text{ }^{\circ}\text{C}$ with the motor participation coefficient in braking equal to 0.25 and $T_{Cu} = 185\text{ }^{\circ}\text{C}$ with the motor participation coefficient in braking equal to 0.1. These temperatures are relatively high, exceeding the operating temperature of the epoxy resin used at the Institute. If the cycle is repeated five times, the maximum winding temperature increases to $T_{Cu} = 250\text{ }^{\circ}\text{C}$, while in the second repetition of the driving cycle, the temperature is already significantly higher than the permissible insulation temperature.

The motor with the shortest package should not operate in a repeated dynamic cycle. In the first repetition of the cycle, the motor with a package length $L_{Fe} = 50\text{ mm}$ reaches the maximum winding temperature of approximately $T_{Cu} = 155\text{ }^{\circ}\text{C}$; in the next cycle, $T_{Cu} = 170\text{ }^{\circ}\text{C}$, and then it reaches $T_{Cu} = 180\text{ }^{\circ}\text{C}$. If regenerative braking is limited, temperatures in subsequent cycles are additionally reduced by $\Delta T_{Cu} = 10\text{ }^{\circ}\text{C}$. This temperature is

significantly lower and is safe for grooved insulation and winding wire. It does not exceed the permissible operating temperature of the epoxy resin used.

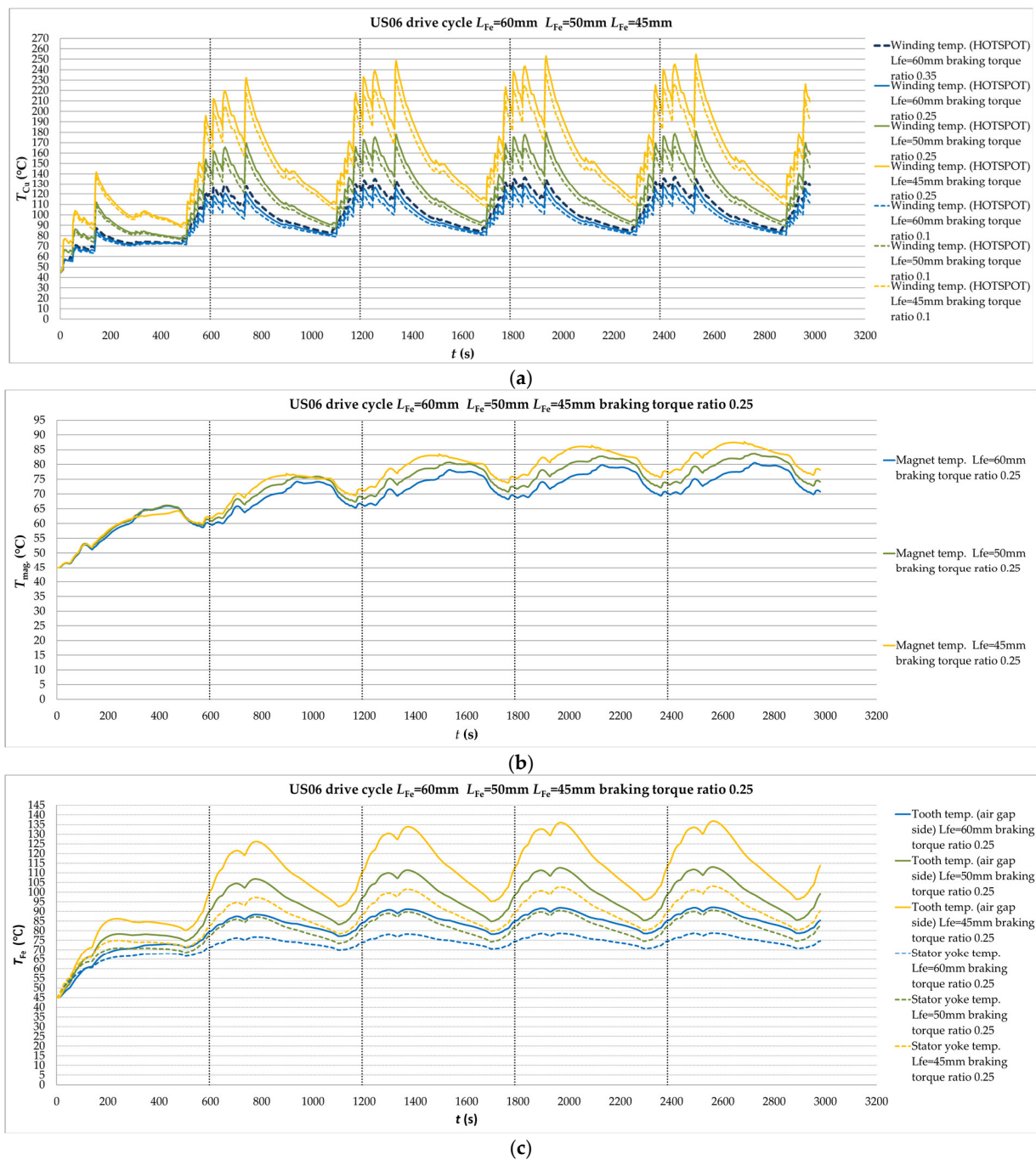
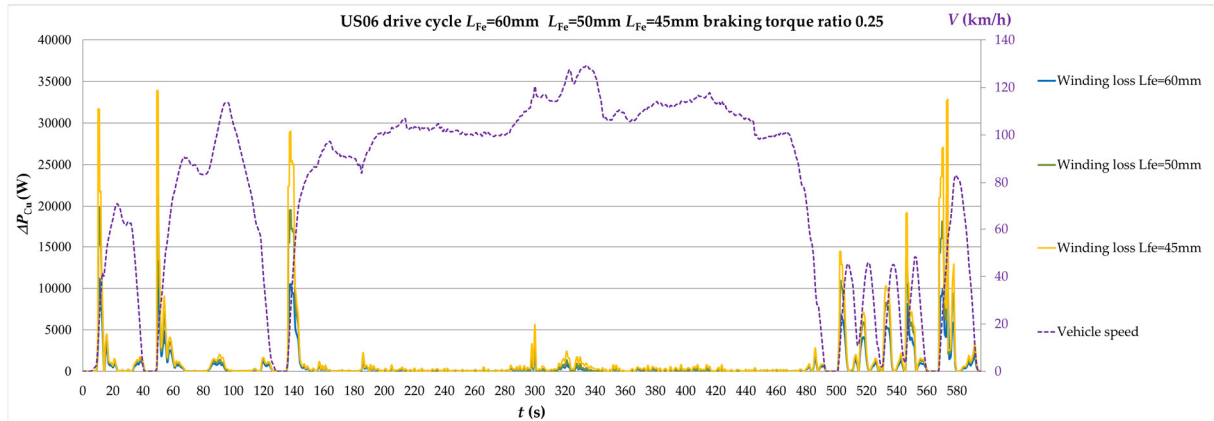


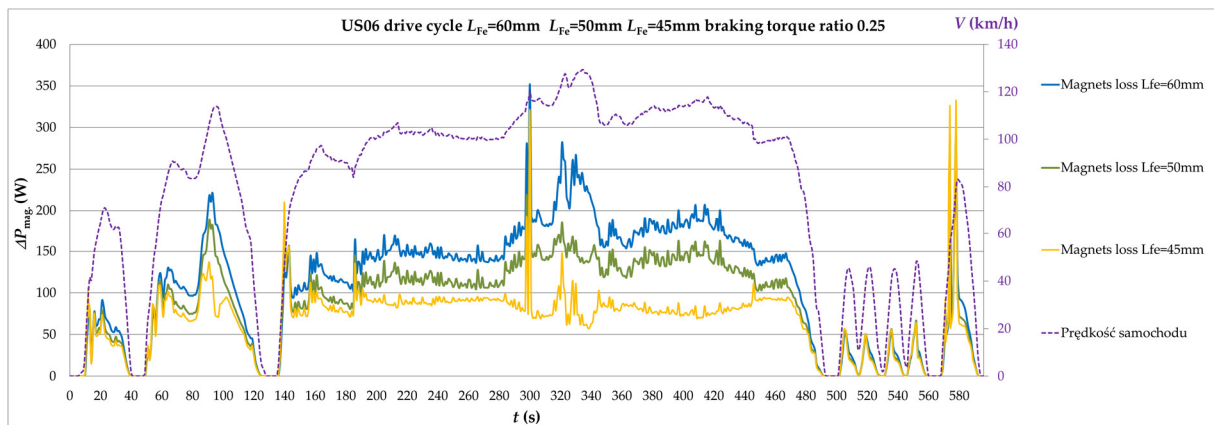
Figure 22. Calculated temperature course of individual motor components in the considered Nissan Leaf car with a drive with two motors in the wheels, moving in the US06 driving cycle repeated 5 times (motor participation coefficient at the moment of braking 0.25). Waveforms for three lengths of magnetic cores: (a) maximum winding temperature, (b) magnet temperature, (c) stator magnetic core temperature.

In the case of the motor with the longest magnetic core, the maximum winding temperature, even when the cycle is repeated five times, does not exceed $T_{Cu} = 130\text{ }^{\circ}\text{C}$. It is also possible to increase the motor's share in braking the car to 0.35 of the total braking torque, without exceeding the temperature $T_{Cu} = 140\text{ }^{\circ}\text{C}$.

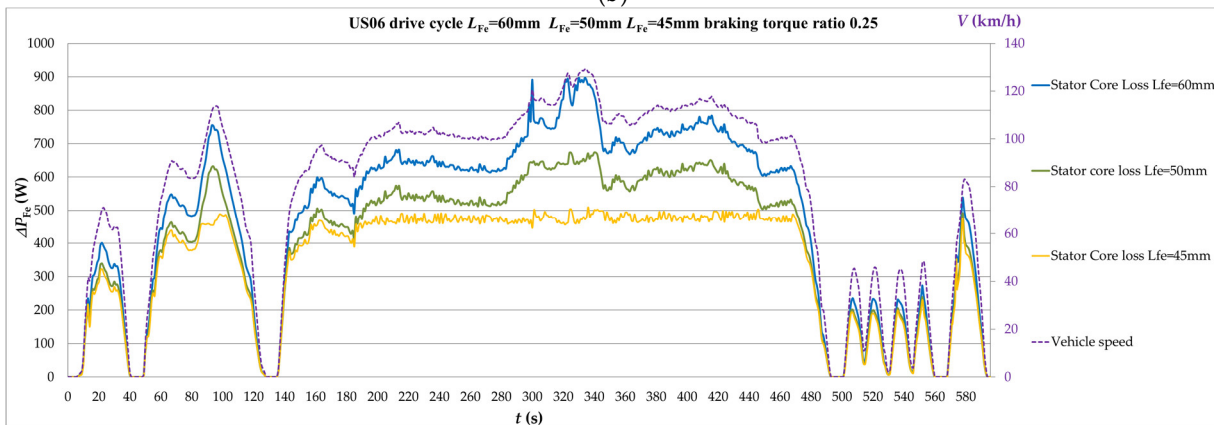
The temperature patterns of the magnets are influenced by the transition to the second control zone. For example, in the first driving cycle, after 300 s, the temperature increase rate is limited and then it decreases. This phenomenon is illustrated by the course of losses in magnets shown in Figure 23, the value of which first stabilizes and then decreases.



(a)



(b)



(c)

Figure 23. The course of individual losses of the electromagnetic circuit of the motor in the considered Nissan Leaf car during a drive with two motors in the wheels, moving in the US06 driving cycle repeated 5 times (motor participation coefficient at the moment of braking 0.25). Waveforms for three lengths of magnetic cores: (a) in the winding, (b) in the magnets, (c) in the stator magnetic core.

With subsequent repetitions of driving cycles, the temperature ratio of the magnets of the considered motors changes. In the first cycle, the motor with the shortest core has the

lowest magnet temperature, then in subsequent cycles, the temperature of the magnets of this motor increases in relation to the other motors and finally reaches the highest value. This is the result of three factors: an increase in the initial temperature of the permanent magnets of each repetition, an increase in the temperature of the winding and the magnetic core, which transfer part of the heat to the rotor, and the fact that as the temperature of the permanent magnets increases, their operating point changes and the magnet requires less field weakening (lower current I_d), which reduces the scope for limiting power losses and necessitates a larger current to generate the required torque (higher current I_q).

For a motor with a package length of $L_{Fe} = 45$ mm, the stator yoke temperature changes from $T_{Fe} = 75$ °C in the first repetition of the cycle to $T_{Fe} = 103$ °C in the fifth repetition of the cycle. For a motor with $L_{Fe} = 50$ mm, the maximum stator yoke temperature varies from $T_{Fe} = 70$ °C to $T_{Fe} = 90$ °C, while when $L_{Fe} = 60$ mm, the stator yoke temperature varies from $T_{Fe} = 68$ °C to $T_{Fe} = 78$ °C. Such an analysis of the yoke temperature is important due to the design of the motor with an external rotor because too large a temperature difference between the stator yoke and the aluminum supporting structure (on which it is mounted) may lead to a deterioration of the contact between these two elements and a reduction in heat collection from the winding, and, as a consequence, motor failure due to thermal reasons or cracking of the resin caused by too much stress as a result of various thermal expansions of the materials.

5. Changing the Number of Motor Pole Pairs

In order to reduce the weight of the motor, in addition to using light and durable materials for the construction of the supporting structure, hull and anchor shield, it is necessary to reduce the weight of the electromagnetic circuit as much as possible, as it usually constitutes more than 50% of the weight of the entire motor. Shortening the electromagnetic circuit package reduces weight but also reduces the motor operating range.

Another direction to reduce the mass of an electromagnetic circuit is to increase the number of pairs of magnetic poles. When designing an electromagnetic circuit, one should strive to obtain as many magnetic poles as possible, which allows for a reduction in the volume of the electromagnetic circuit due to the smaller magnetic flux in the area of a single pole. As a result, the width of the stator yoke and the rotor yoke of the magnetic circuit can be significantly reduced, which gives a more favorable ratio of the volume and mass of the core to the rated torque.

When considering the possibilities of reducing the mass of an electromagnetic circuit by increasing the number of pole pairs, attention should be paid to a number of existing limitations. Increasing the number of poles in SPM motors is technologically simple but may be limited by the minimum dimensions of a single magnet. Another limitation is the maximum voltage frequency with which the used inverter can supply the motor. It should also be remembered that when the yoke thickness is reduced, the mechanical strength of the rotor decreases. Another limitation is the voltage induced by the magnetic flux of permanent magnets when the machine is operating at idle speed, which should not exceed the so-called non-operating voltage of the inverter. If the driver loses control of the motor while operating at maximum speed, exceeding this voltage during generator operation at idle speed of the motor may result in damage to the inverter. Increasing the number of pairs of magnetic poles also affects the number of stator slots and the number of winding coils, which consequently results in a reduction in the width of the stator teeth. The limitation is the minimum bending radius of the coil and ensuring its feasibility and the cost of building the winding. Another limitation of the increase in the number of pairs of magnetic poles is introduced by the speed measurement sensor used (usually an encoder or resolver), the stable operation of which may be difficult due to the resolution range.

An additional problem arises when, as the number of poles increases, we want to proportionally increase the number of stator slots. For example, in a motor with the number of poles $2p = 32$ and the number of slots $Q_s = 48$, the number of slots per pole and phase is $q = 0.5$. If we increase the number of poles to $2p = 56$, to maintain $q = 0.5$, the number

of slots would have to increase to $Q_s = 84$. Given the imposed external dimensions of the motor, such a large number of slots may be impossible or unreasonable to use due to the technological limitations of the machinery (as the number of slots increases, their cross-section decreases). Additionally, the cost of making the winding also increases due to the increasing number of coils that need to be made and then connected. The active cross-section of the nursery also decreases because as the number of nurseries increases, the share of nursery insulation increases.

A solution may be to reduce the number of slots per pole and phase:

$$q = Q/2p \cdot m$$

where Q —is the number of stator slots; m —number of motor phases; and $2p$ —number of magnetic poles.

However, it should be remembered that for motors where $q < 0.5$, the spatial distribution of the magnetomotive force is distorted, which causes an increase in eddy current losses in permanent magnets [70].

Typically, in electric motors, the factor limiting the torque is the winding temperature, limited by the permissible insulation temperature. In the case of multi-pole motors, especially with the number of slots per pole and phase q equal to or less than 0.5, increased losses in the permanent magnets may cause the temperature of the magnets to limit the maximum load of the motor, especially when the motor is running at the so-called de-excitation to increase the rotational speed range [71]. During de-excitation, the magnets are exposed not only to an increase in temperature caused by power losses depending on the supply current and frequency but also to the action of an external magnetic field. Selecting a fractional number of slots per pole and phase can significantly reduce the cogging torque of the motor.

There are many publications on the selection of the number of slots per pole and phase and various aspects of this selection [72–75].

Therefore, this paper focuses on comparing the operating parameters and temperatures of the motor in relation to the requirements for a car drive.

Increasing the number of pairs of magnetic poles allows you to obtain a toroid-shaped motor that increases its internal diameter. In this way, in addition to reducing weight, you also gain additional space for installing, for example, a brake drum, suspension elements or a braking system.

Another advantage of increasing the number of pairs of magnetic poles and the number of stator slots is a smaller coil cross-section and a shorter overhang of the winding ends, which allows us to shorten the length of the supporting structure and the entire motor body or increase the length of the motor package, using the available space for the electromagnetic circuit.

For the analysis, it was assumed that the shortening of the ends would be used to extend the magnetic core package from 60 mm to 65 mm.

The motor with an increased number of pairs of magnetic poles $2p = 56$ was designed in such a way that the maximum torque at the supply current $I_{\text{RMS}} = 350\text{A}$ was comparable to the maximum torque of the mapped motor (Figure 24).

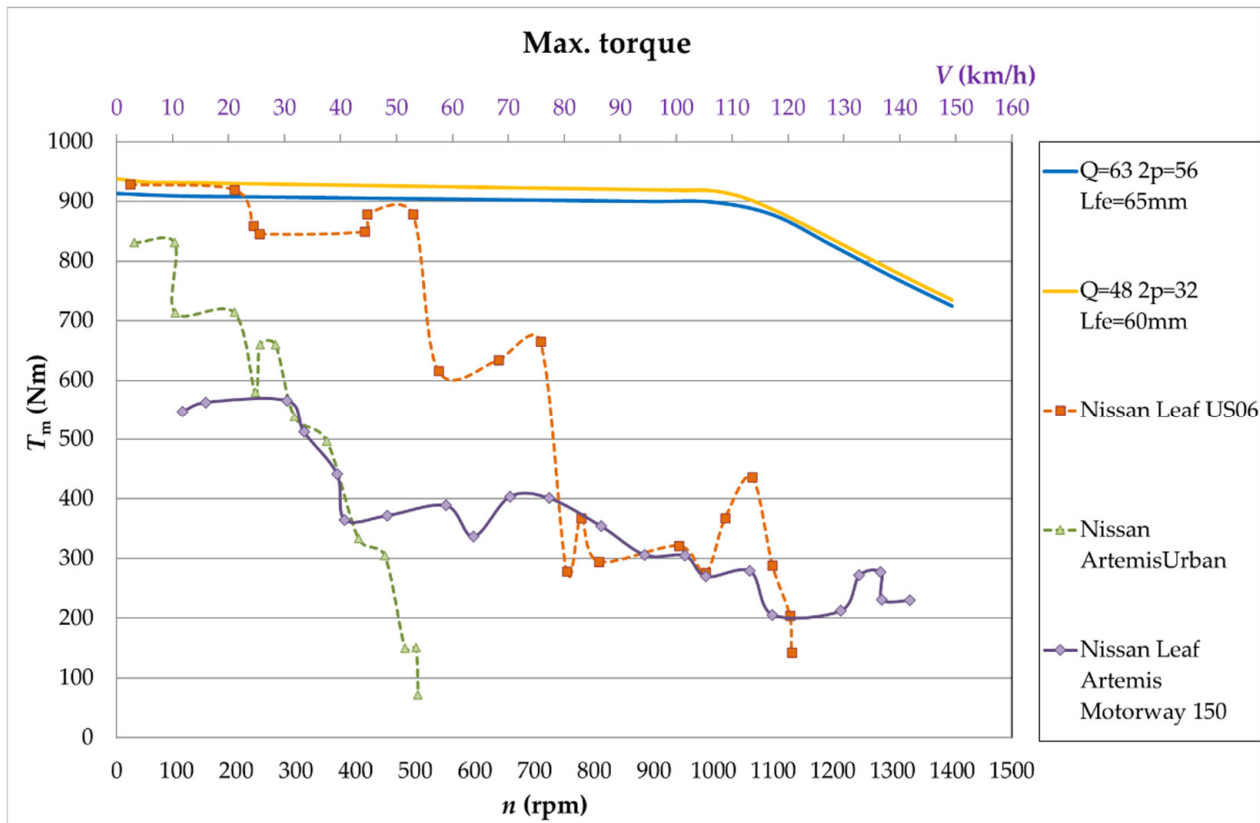


Figure 24. Calculated characteristics of maximum torque as a function of rotational speed of the modeled motor and the motor with an increased number of pole pairs ($2p = 56$ and $q = 0.375$).

The electromechanical characteristics of both motors are very similar throughout the entire operating range. The difference in torque does not exceed 2%, assuming that the magnets in both motors operate at the same temperature. Table 8 shows a comparison of the mass of the electromagnetic circuit elements of both motors. The electromagnet circuit with an increased number of pole pairs is characterized by a mass that is 12.5% lower.

Table 8. Comparison of the mass of electromagnetic circuits of motors.

Parameter	Motor 1	Motor 2	Unit
Number of stator slots Q	48	63	-
Number of magnetic pole pairs $2p$	32	56	-
Magnetic core length L_{Fe} , (mm)	60	65	-
Number of stator slots per pole and phase q	0.5	0.375	-
Winding mass	4.5	3.6	kg
Stator core mass	9.5	8.8	kg
Rotor core mass	4.4	3.3	kg
Permanent magnets mass	1.6	1.8	kg
Total mass of the electromagnetic circuit	20	17.5	kg
Stator internal diameter	280	302	mm
Cogging torque	19.5	1.5	Nm

The distribution of magnetic induction in the core of both motor models is shown in Figures 25 and 26 and Table 9. The circuits are comparable in terms of the use of the magnetic core.

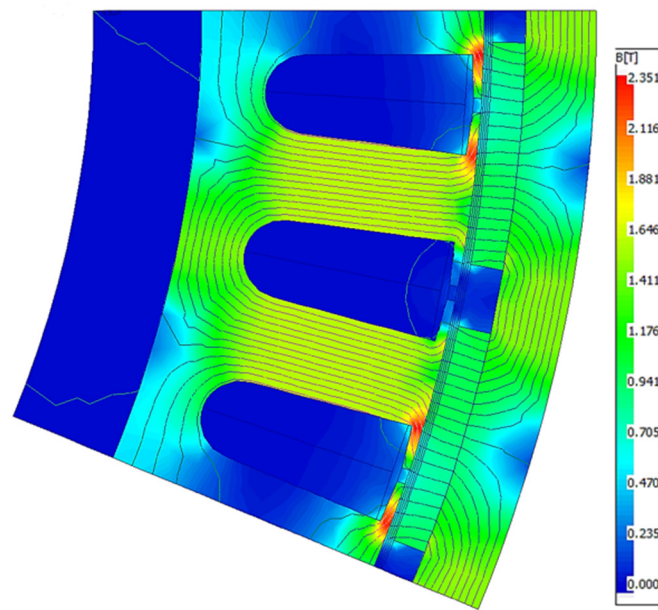


Figure 25. Distribution of magnetic induction from permanent magnets of the considered motor model: $Q = 48$, $2p = 32$, $q = 0.5$.

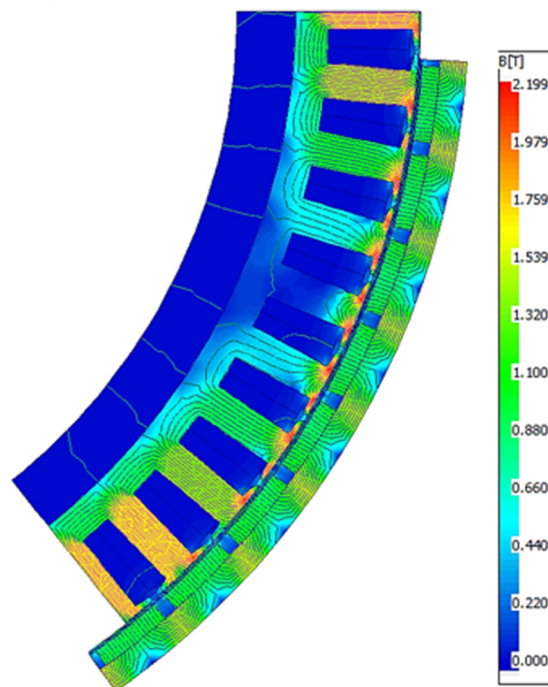


Figure 26. Distribution of magnetic induction from permanent magnets of the considered motor model $Q = 63$, $2p = 56$, $q = 0.375$.

Table 9. Distribution of magnetic induction from permanent magnets ($I = 0$ A).

Magnetic Induction (T)	$2p = 32$	$2p = 56$
In the air gap (average)	0.72	0.8
In the air gap (peak)	1.05	1.03
In the stator tooth (peak)	1.71	1.7
In the upper part of the stator tooth (peak)	2.31	2.16
Stator yoke (peak)	1.12	1.25
Rotor yoke (peak)	1.5	1.45

The voltages from the permanent magnets during no-load generator operation in both motors are very similar. In the case of the modeled motor, this voltage is $U_{\text{Back BMF RMS}} = 178.5 \text{ V}$, while in the case of the considered motor with an increased number of pole pairs, it is $U_{\text{Back BMF RMS}} = 172 \text{ V}$.

In the case of the cogging torque, the differences are greater. In the motor modeled with $q = 0.5$, the cogging torque is $T_{\text{cog.}} = 19.5 \text{ N}\cdot\text{m}$, and in the motor with an increased number of pole pairs and $q = 0.375$, it is $T_{\text{cog.}} = 1.5 \text{ N}\cdot\text{m}$.

For the motor with an increased number of magnetic pole pairs, a model was made for thermal calculations while maintaining the same thermal contact resistances and using the same materials. Figure 27 shows cross-sections of the models of both motors. The model with an increased number of pole pairs, in accordance with the assumptions, is characterized by a larger internal diameter, a slightly shorter overhang of the fronts and a longer magnetic core package of the stator and rotor.

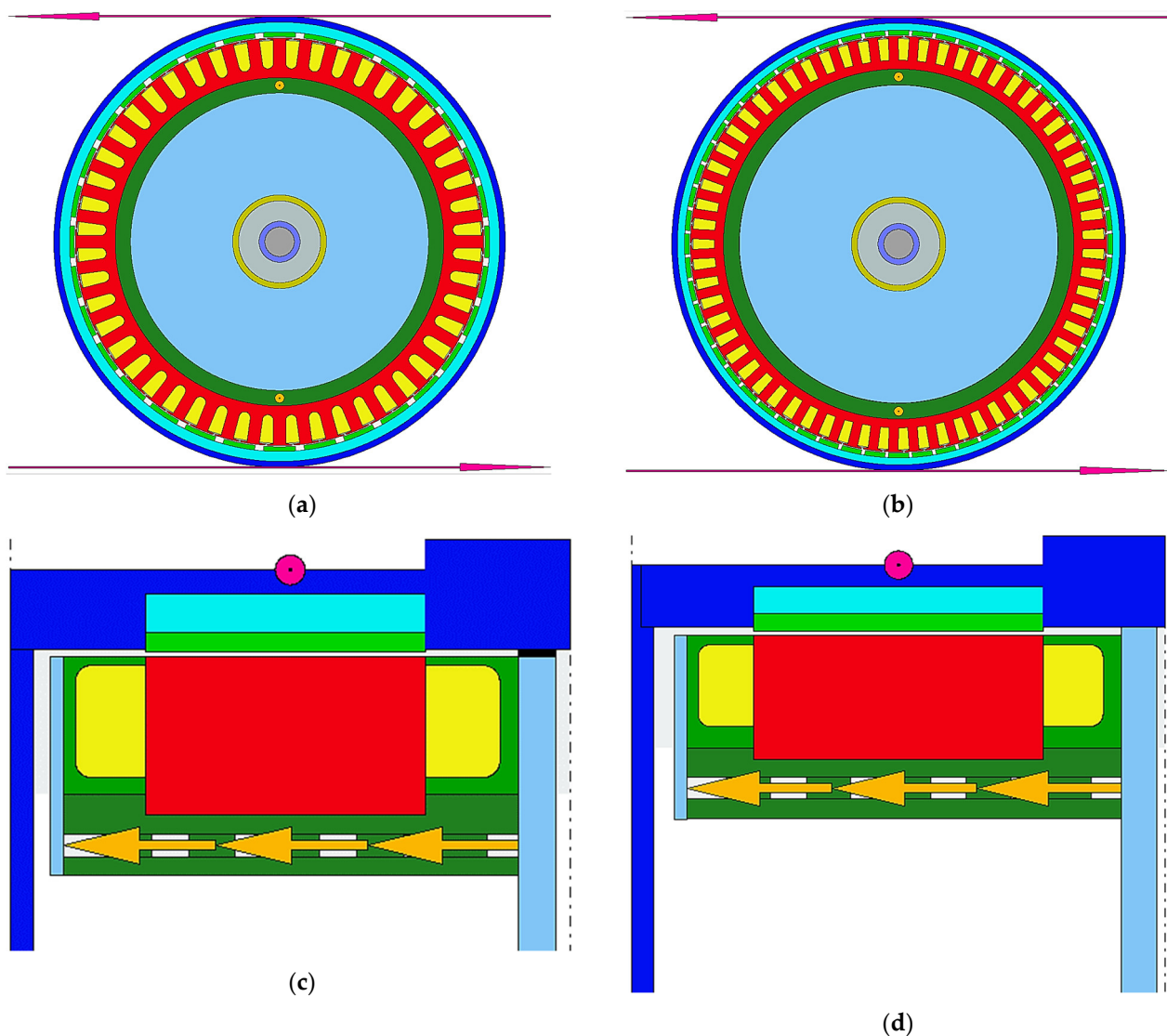


Figure 27. Motor model cross-sections: (a) cross section of the model $2p = 32, q = 0.5$; (b) cross section of the model $2p = 56, q = 0.375$. (c) longitudinal section of the model $2p = 32, q = 0.5$. (d) longitudinal section of the model $2p = 56, q = 0.375$.

5.1. Changing the Number of Motor Magnetic Poles—Artemis Urban Driving Cycle

Figure 28 compares the maximum temperature curves of the winding, permanent magnets and the magnetic core of a motor with the number of magnetic pole pairs $2p = 32$ and $2p = 56$.

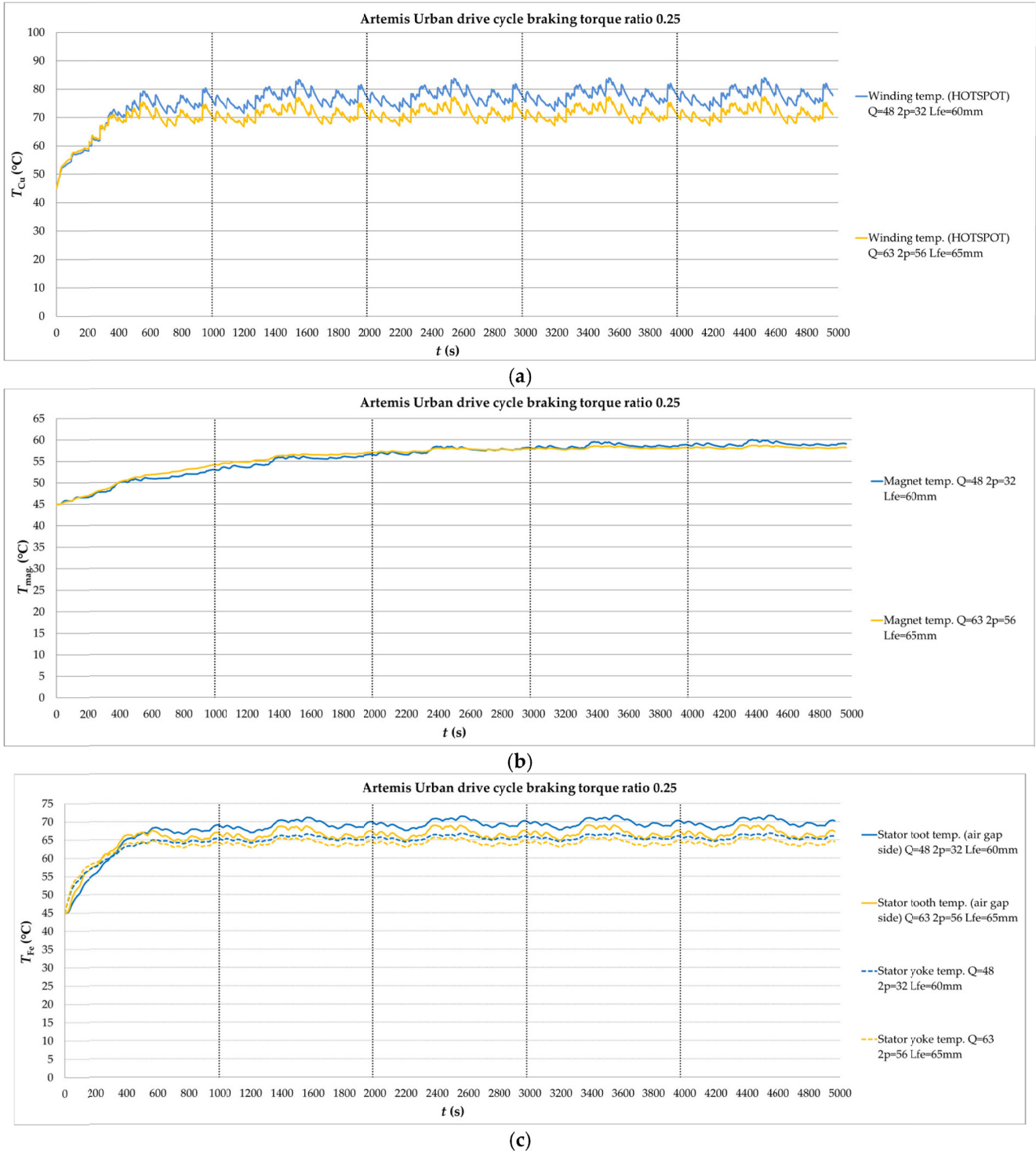
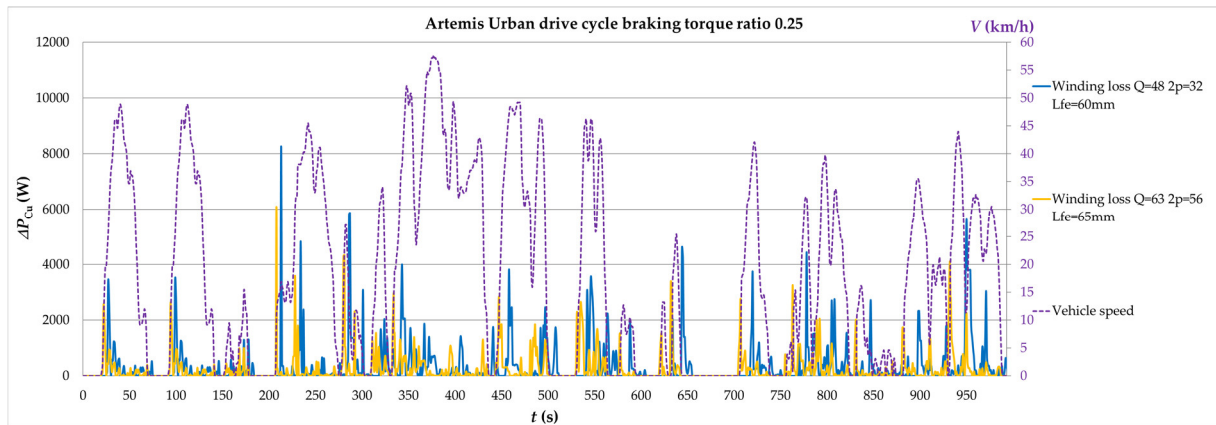


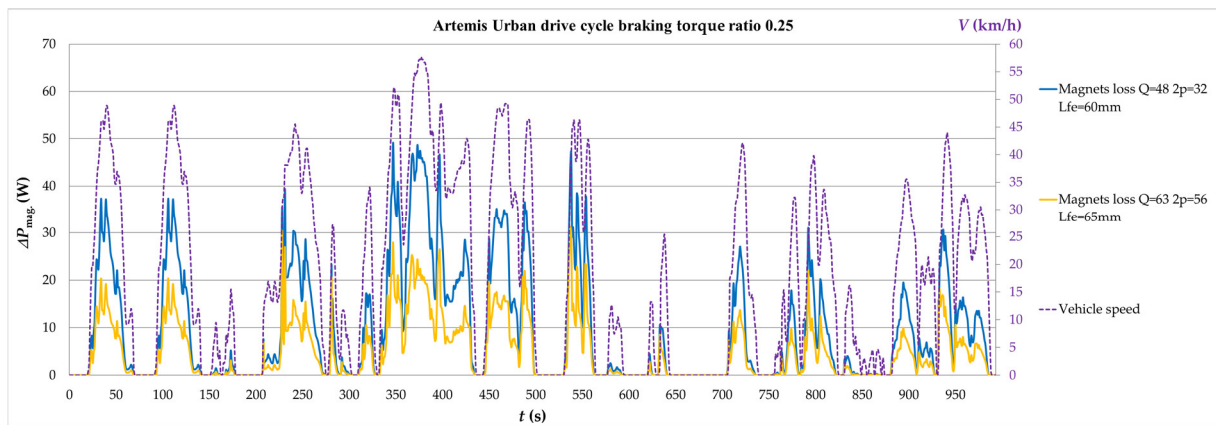
Figure 28. Calculated temperature curves of individual motor components in the considered Nissan Leaf car with dual-motor drive, running in the Artemis Urban driving cycle repeated 5 times (braking torque participation factor 0.25): (a) maximum winding, (b) magnet, (c) stator magnetic core.

The motor with the number of magnetic pole pairs $p = 56$ and a smaller mass of the electromagnetic circuit has a lower operating temperature during urban driving. The difference in maximum temperature in both motors was about $\Delta T = 5\text{ }^\circ\text{C}$. The temperature of the permanent magnets is almost the same. The operating temperature of the stator magnetic core is lower by about $\Delta T = 3\text{ }^\circ\text{C}$ in the motor with the number of pole pairs $2p = 56$.

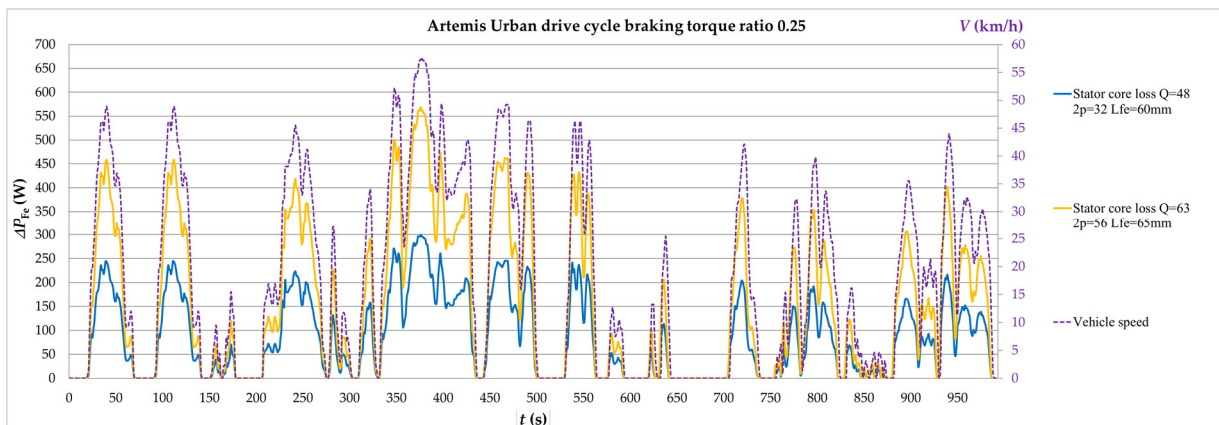
Figure 29 shows the power loss curves in the elements of both motors in the Artemis Urban cycle. In the motor with $2p = 32$, the losses in the winding and permanent magnets are greater, while in the stator magnetic core, they are smaller.



(a)



(b)



(c)

Figure 29. Calculated motor power loss curves for a Nissan Leaf with dual-wheel drive, running in the Artemis Urban driving cycle: (a) winding, (b) magnet, (c) stator magnetic core.

5.2. Changing the Number of Motor Magnetic Poles—Artemis Motorway 150 Driving Cycle

The analysis of the car’s driving in the Artemis Motorway 150 cycle showed that the maximum winding temperature in the cycle is equal to about $T_{Cu} = 87\text{ }^{\circ}\text{C}$ (Figures 30 and 31) for both motors, but its courses during the cycle are different.

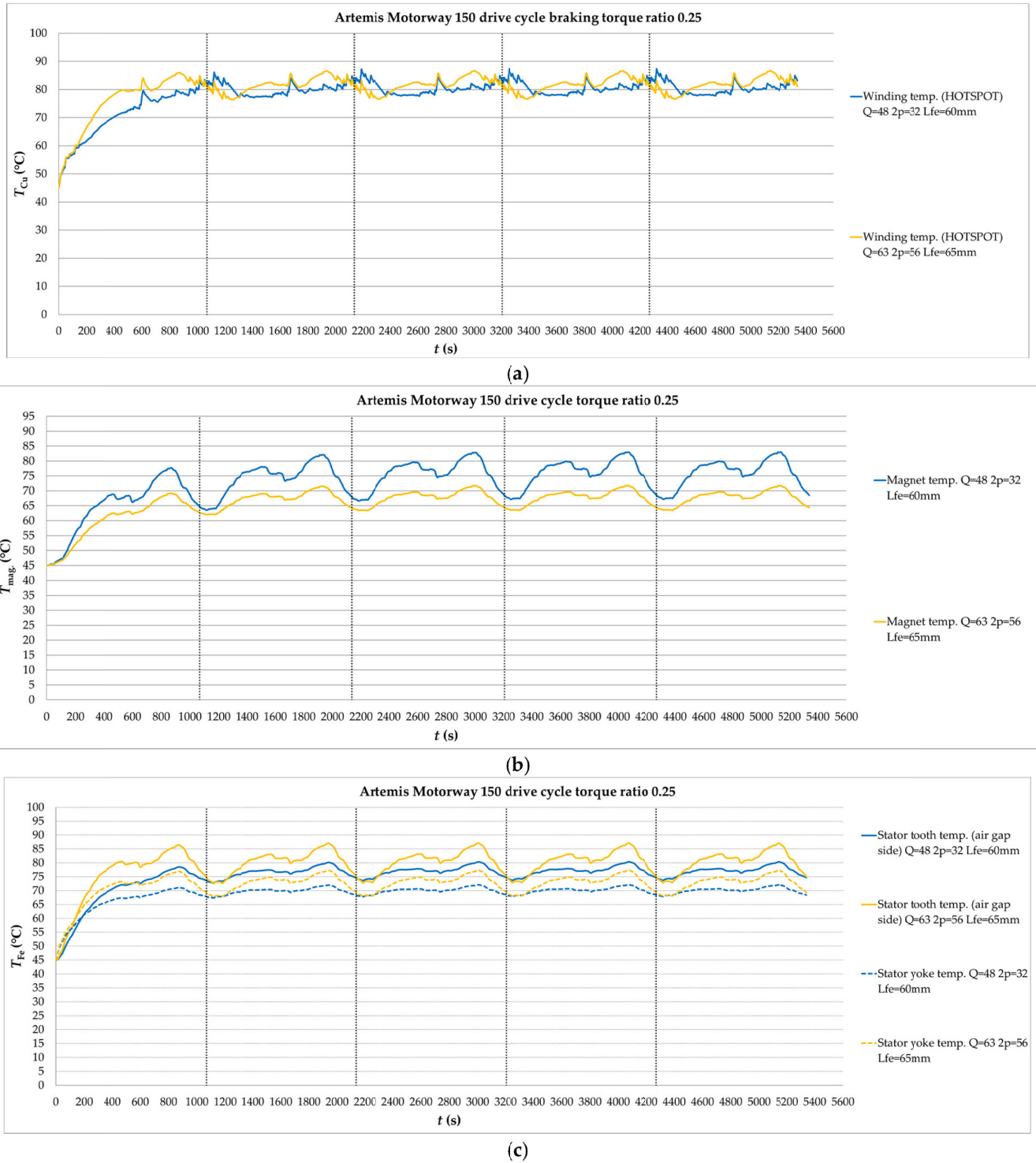


Figure 30. Calculated temperature curves of individual motor components in the considered Nissan Leaf car with dual-motor drive, running in the Artemis Motorway 150 driving cycle repeated 5 times (braking torque participation factor 0.25): (a) maximum winding, (b) magnet, (c) stator magnetic core.

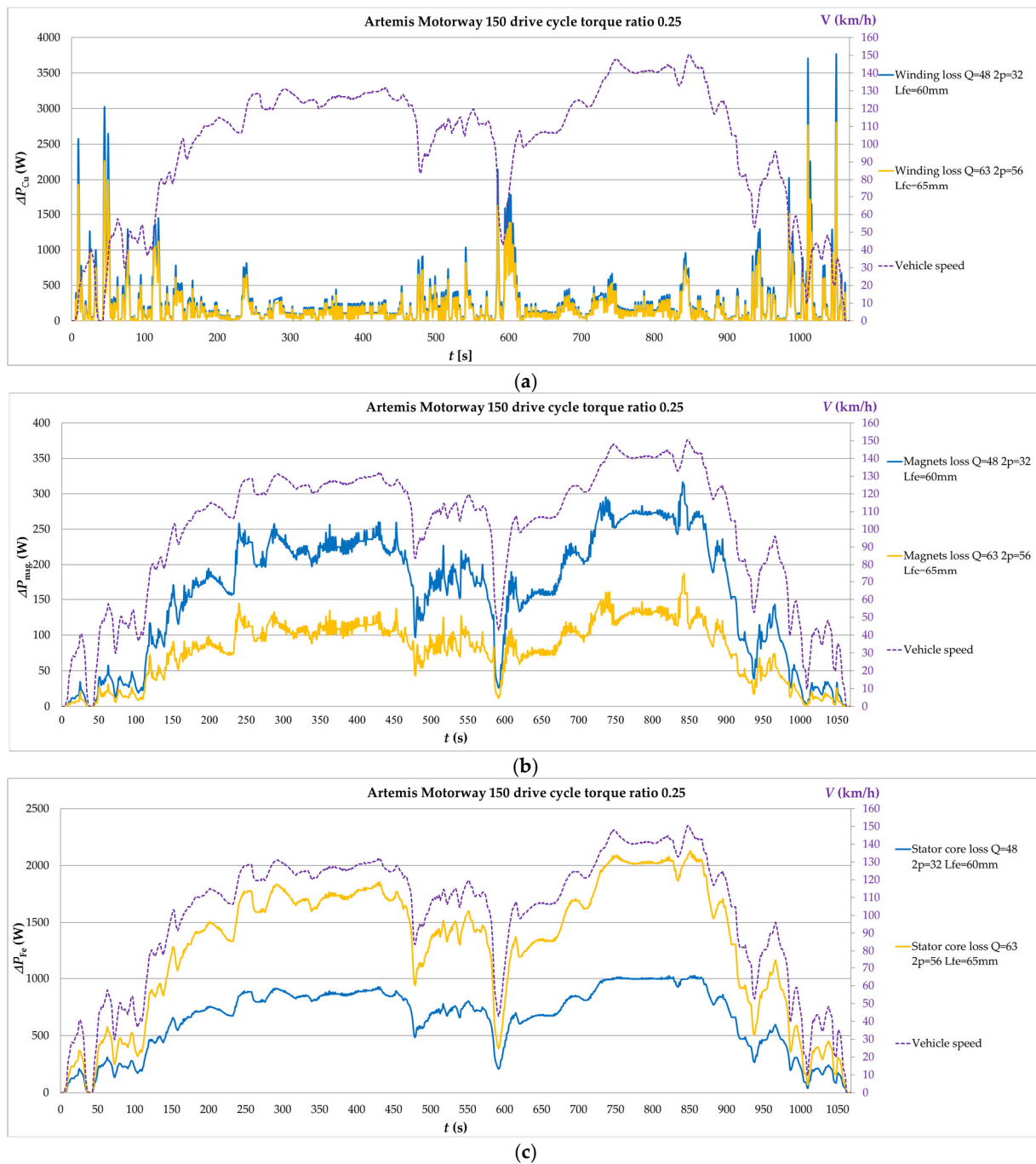


Figure 31. Calculated motor power loss curves for the considered Nissan Leaf vehicle with dual-motor in-wheel drive, operating in the Artemis Motorway 150 driving cycle: losses in (a) winding, (b) magnets, (c) stator magnetic core.

Higher temperatures are obtained by the motor with the number of magnetic poles $2p = 32$ at the beginning and end of the cycle, when entering and leaving the motorway. In turn, the motor with an increased number of magnetic pole pairs of $2p = 56$ operates with a higher maximum temperature while the car is driving at a higher speed. The core temperature, analogously to the course of power losses in the core, is higher in the motor with the increased number of pole pairs. The operating temperature of permanent magnets is more than $\Delta T_{mag} = 10^\circ\text{C}$ lower when the car is driving at higher speeds, about $V = 130$ km/h.

5.3. Changing the Number of Magnetic Poles of the Motor—US06 Driving Cycle

The analysis of the dynamic driving cycle (Figures 32 and 33) showed that the maximum winding temperatures were higher in the motor with the number of magnetic poles $2p = 32$, even by as much as $\Delta T = 17\text{ }^\circ\text{C}$ in the last repetition of the cycle.

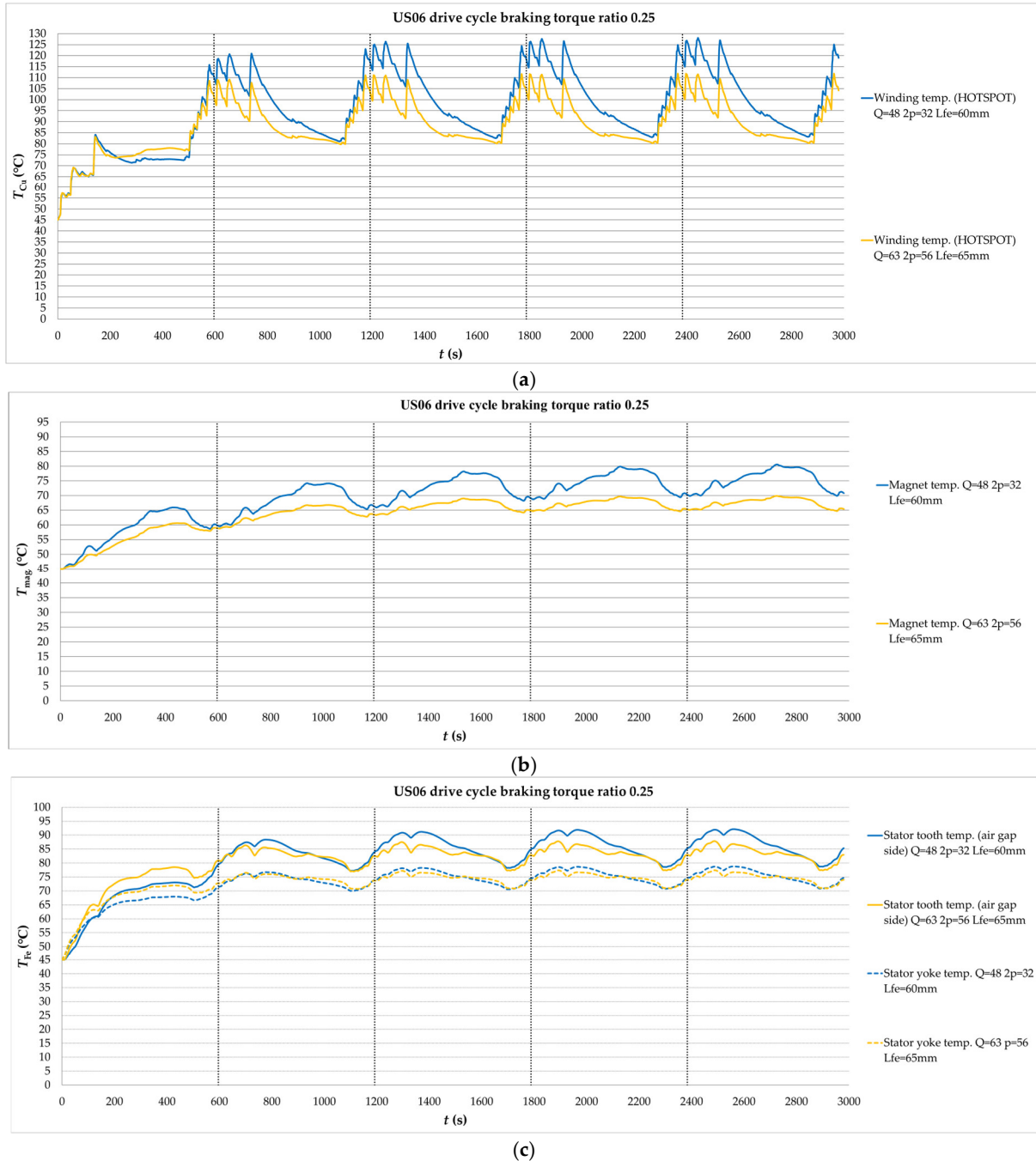


Figure 32. Calculated temperature curves of individual motor components in the considered Nissan Leaf car with dual-motor drive, running in the US06 driving cycle repeated 5 times (braking torque participation factor 0.25): (a) maximum winding, (b) magnet, (c) stator magnetic core.

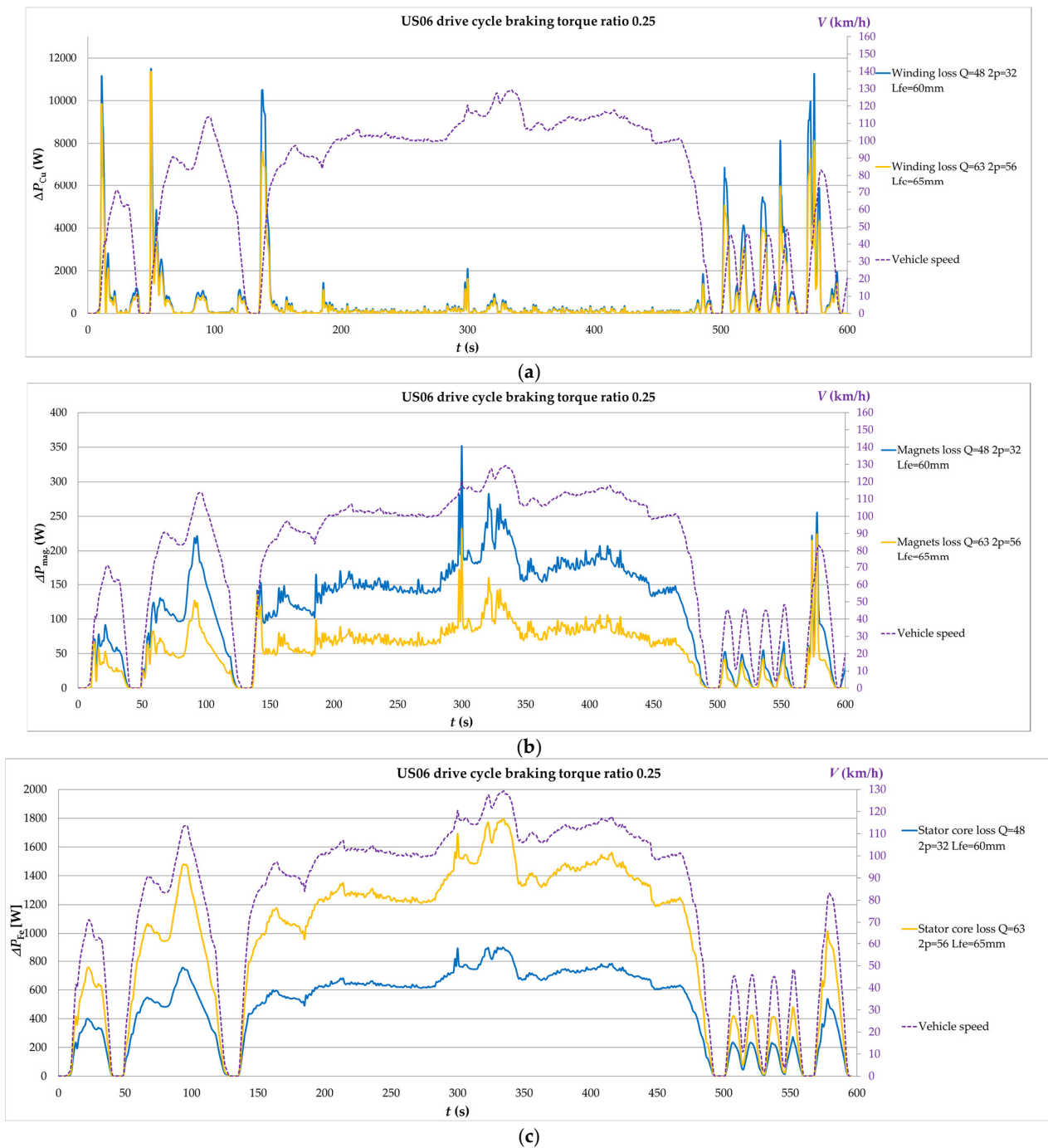


Figure 33. Calculated power loss curves of the motor in the considered Nissan Leaf car with a dual-motor drive, moving in the US06 driving cycle repeated 5 times (motor participation factor in the braking moment 0.25): (a) in the winding, (b) in the magnets, (c) in the stator magnetic core.

Simulations have shown that the $2p = 32$ motor achieves higher temperatures when driving at low speeds and high torque. In the case of driving at higher speeds in the US06 cycle, in the first repetition of the cycle, the temperature of the $2p = 56$ motor is slightly higher, while in the next repetitions, the influence of the temperature at the beginning of the cycle is visible, which changes this relationship in the subsequent repetitions. The temperature of the permanent magnets is higher in the $2p = 32$ motor throughout the cycle.

6. Conclusions

6.1. Discussion on Results

The research shows that the most intuitive axial shortening of the magnetic core of the motor allows for a relatively large reduction in length and the mass of the electromagnetic circuit (Table 7) but is associated with a limitation of operating parameters due to temperature reasons. With the shortening of the magnetic core length, the axial dimension of the motor is shortened, while its thermal load increases throughout the entire operating range (Figures 18a, 20a and 22a).

In the first motor control zone (constant torque zone), the thermal load increases. This is the result of the need to increase the number of winding turns at the expense of the wire cross-section and increase the current density. In this way, the length of the magnetic core is shortened, while the maximum torque is maintained, and in the second motor control zone (in the zone of weakened permanent magnets) the additional load increases the range of flux weakening. Shortening the package and the necessary change in the winding in order to provide the required torque causes the base point of the motor characteristic to shift to lower rotational speeds.

Increasing the range of operation with field weakening during the driving cycle results in an increase in the I_{RMS} current.

During city driving, in the Artemis Urban cycle (Figure 16a), the maximum winding temperature courses differed in value, while the shape of the course itself was the same for all three magnetic core lengths. The reason is that for all three versions of the motor, with different lengths of the magnetic core considered, this cycle is carried out in the first control zone (Figure 17).

For the motorway driving cycle (Figure 16b), the graphs differ not only in value. The maximum operating temperature for the shortest motor occurs at a different time moment when the car is driving at the highest speed (Figure 20a). The differences in the courses deepen with the increase in the range of operation of the motor with weakening of the magnetic field of permanent magnets (Figure 17).

The temperature of permanent magnets during city driving (Figure 18b) is slightly higher in motors with the shortest package, while the situation is the opposite when driving on the motorway (Figure 20b). The increased range of field weakening causes a reduction in the power losses generated in permanent magnets (Figure 21b) and a reduction in the operating temperature of the magnets.

In the dynamic cycle (Figure 16c), the main difference is the maximum stator winding temperature (Figure 22a), which reaches high values during vehicle acceleration after a series of rapid accelerations and decelerations at the beginning of the driving cycle and during dynamic maneuvers at the end of the driving cycle.

It may be noted that although the wheel hub motor with the shortest magnetic core is able to generate the torque required by the US06 duty cycle (Figure 17), the winding operating temperatures reach $T_{Cu} = 190$ °C in the first repetition and up to $T_{Cu} = 250$ °C in subsequent repetitions of the cycle. The winding temperature is limited not only by the permissible operating temperature of the insulation but also by the epoxy resin in which the wound motor stator is encapsulated (Figure 1). The analysis gives information that such dynamic driving may occur occasionally or in cases of emergency. The drive with the shortest magnetic core does not allow for constant, very dynamic driving.

A large temperature difference can also be seen in the stator magnetic core (Figure 22c), where the difference in the dynamic cycle between the $L_{Fe} = 60$ mm and $L_{Fe} = 45$ mm packages is about $\Delta T = 40$ °C in the tooth and about $\Delta T = 24$ °C in the stator yoke when the cooling liquid at the motor shaft is the same temperature. The high temperature of the magnetic core is dangerous for the motor structure because it can introduce stresses that can lead to cracking of the epoxy resin and can increase the contact resistance between the stator and the structure on which the stator is mounted, causing a significant deterioration in heat dissipation from the winding.

Increasing the number of pole pairs from 32 to 56 resulted in a reduction in the mass of the electromagnetic circuit by over 12% and the creation of additional space inside the wheel by increasing the internal diameter of the motor (Figure 24, Table 8).

The motor with an increased number of magnetic pole pairs and $q = 0.375$ is characterized by a significantly lower cogging torque (Table 8), which in the case of an electric vehicle drive can have a significant impact on the comfort of driving and controllability of the vehicle. To reduce the value of the cogging torque, a skew in the stator or a discrete skew of the rotor magnets can be used. However, this is associated with a reduction in torque and the need to increase the supply current, which will increase the working temperature of the winding and result in an even greater temperature difference in favor of the motor with an increased number of magnetic pole pairs.

The new proposal for the electromagnetic circuit seems to be more advantageous both in terms of mass and thermal parameters. It opens up the possibility of shortening the package and, consequently, an even greater reduction in the mass of the electromagnetic circuit and also a reduction in the axial length of the motor.

The maximum operating temperature of the motor with an increased number of magnetic pole pairs during the Artemis Urban cycle is approximately $\Delta T = 10$ °C lower. The temperatures of the magnetic core and magnets are similar (Figure 28).

During the Artemis Motorway 150 cycle, the winding temperature of the motor with an increased number of magnetic poles is higher when driving at speeds above $V = 100$ km/h by approximately $\Delta T = 10$ °C and is lower at lower vehicle speeds (Figure 30a). The variable advantage of the winding temperature between the compared motors in this duty cycle is influenced by the dependence of the winding temperature on the temperature of the magnetic core and indirectly generated power losses in the magnetic core (Figure 31c).

The temperature of the permanent magnets in the motor with a smaller number of magnetic poles is higher (Figure 30b), which correlates with the calculated power losses in the magnets for this driving cycle (Figure 31b).

The maximum operating temperature of the winding and permanent magnets is also higher in the motor with a smaller number of magnetic pole pairs in the dynamic driving cycle under consideration (Figure 32a).

During the first repetition of the US06 cycle, the motor with an increased number of magnetic pole pairs is characterized by a slightly higher winding temperature in the middle part of the cycle (Figure 32a). During this time, the car moves at a higher speed, which results in a greater impact on the winding temperature of the losses generated in the stator magnetic core (Figure 33c). This situation does not repeat in the following cycle repetitions because the motor winding with fewer magnetic pole pairs starts the cycle at a higher temperature.

The analysis showed that increasing the number of magnetic pole pairs can provide additional space in the vehicle wheel (Table 8), e.g., for the installation of a drum brake, and can reduce the motor mass while maintaining the operating temperature at a safe level; in various driving scenarios, it even lowers the temperature. Changing the core length while maintaining the maximum torque at the required level effectively reduces the axial dimension of the machine and the motor mass while increasing the current density in the entire motor operating range and increasing the motor operating area with weakening of permanent magnets, which additionally increases the current load. The simulation analysis performed allowed for the visualization of the effect of these changes on the motor operating temperature and detection of the situations in which the operating temperatures reach unacceptable values.

6.2. Conclusions—Summary

The article presents the most important issue in the field of designing motors for installation in a car wheel, which is the search for methods to reduce its dimensions and weight while meeting very high requirements regarding motor parameters, in particular, obtaining the highest possible torque. Modern simulation tools were used for the research

to determine the operating parameters of an electric motor operating in a car in various conditions occurring during typical city driving, on the motorway and dynamic driving, not assuming a constant motor load (as is often the case in other studies).

The analysis carried out allowed us to draw attention to the operating parameters of the wheel hub motor while driving the car, taking into account the design changes that lead to changes in the overall dimensions of the motor and its mass.

To carry out the analysis, a prototype wheel hub motor was made to take into account the actual dimensions and the real structure of the wheel hub motor, which is intended for use in a car. The motor prototype was also used to verify the calculations and calibrate the computational model. Carrying out the analysis on realistic driving cycles made it possible to check what temperature curves will be achieved with changes in the design of the electromagnetic circuit.

The analysis concerned the direction of redesigning the electromagnetic circuit of the wheel hub motor in order to check the possibility of reducing its weight and obtaining additional space in the car rim. This space may limit the motor design in the axial direction and on the inside diameter side. Calculations showed that shortening the length of the magnetic core resulted in an increase in the winding temperature during city and highway driving but without exceeding very high temperatures. The highest winding temperatures were reached by the motors during dynamic driving in the US06 cycle. The combination of deep field weakening when driving the car at high speed and dynamic maneuvers at the beginning and end of the cycle caused the winding temperature to significantly exceed 180 °C.

The motor with the shortest magnetic core cannot operate with such dynamic driving. Another danger that was noticed in the calculations for this motor is the high temperature increase in the magnetic core. This may result in an increase in thermal resistance between the stator magnetic core and the cooling system and cracking of the epoxy resin.

Increasing the number of magnetic poles and redesigning the electromagnetic circuit allowed the internal diameter of the motor to be increased and its weight to be reduced without significantly affecting the temperature of individual motor components.

In addition to the winding, permanent magnets are important elements exposed to temperature. The permissible operating temperature of permanent magnets is lower when they are under the influence of an external magnetic field directed opposite to the magnet field. This situation occurs when the motor is operating in the second control zone, i.e., at a higher rotor speed, which is equivalent to the vehicle moving at a higher speed. The magnet temperature depends on the motor's power supply frequency and its load resulting from the variable dynamics of the vehicle's movement. The analysis of motor operation during real driving cycles, based on a calibrated electromagnetic and thermal-flow model, allows for the assessment of the safety of the operating temperature of the rotor permanent magnets in both control zones.

Power losses depend not only on the power supply parameters but also on the temperature of individual motor components. Without conducting an analysis, as proposed by the authors of the article, it is difficult to predict in what conditions the wheel hub motor will operate and which of its components may fail while the car is driving.

Author Contributions: P.D.—development of computational models, running simulation, designing electromagnetic circuits, analysis of simulation results and preparation of the article. R.K.—analysis of simulation results, participation in the creation of proposals, and editing of the article. All authors have read and agreed to the published version of the manuscript.

Funding: The research is a continuation of the project “Innovative Solutions for Direct Drive of Electric Vehicles”, financed by the National Centre for Research and Development under the LIDER VII program, in accordance with the agreement: LIDER/24/0082/L-7/15/NCBR/2016 (POLAND). The project received the Research Award (main award) 25th Siemens Award Competition for scientists and research teams (Poland).

Data Availability Statement: The original contributions presented in the study are included in the article, further inquiries can be directed to the corresponding author.

Conflicts of Interest: The authors declare no conflicts of interest.

References

1. Irimescu, A.; Mihon, L.; Pădure, G. Utomotive transmission efficiency measurement using a chassis dynamometer. *Int. J. Automot. Technol.* **2011**, *12*, 555–559. [[CrossRef](#)]
2. Rahnejat, H.; Theodossiades, S. Drivetrain Noise, Vibration, and Harshness. In *Encyclopedia of Automotive Engineering*; John Wiley & Sons, Ltd.: Hoboken, NJ, USA, 2014. [[CrossRef](#)]
3. Mohammadpour, M.; Theodossiades, S.; Rahnejat, H.; Kelly, P. Transmission efficiency and noise, vibration and harshness refinement of differential hypoid gear pairs. *Proc. Inst. Mech. Eng. Part K J. Multi-Body Dyn.* **2014**, *228*, 19–33. [[CrossRef](#)]
4. Freitag, G.; Schramm, M. Electric wheel hub motor with high recuperative brake performance in automotive design. *World Electr. Veh. J.* **2012**, *5*, 510–513. [[CrossRef](#)]
5. Glinka, T. *Maszyny Elektryczne Wzbudzone Magnesami Trwałymi*; Wydawnictwo Naukowe PWN: Warszawa, Poland, 2018.
6. Gieras, J.F. *Permanent Magnet Motor Technology: Design and Applications*, 3rd ed.; Taylor & Francis Inc.: Abingdon, UK, 2009.
7. Białas, A.; Będkowski, B.; Dukalski, P.; Radwański, W.; Fręchowicz, A. Koncepcja napędu z silnikiem BLDC o przeczalnej liczbie zwojów w napędzie samochodu elektrycznego. *Przegląd Elektrotechniczny* **2013**, *10*, 194.
8. Glinka, T.; Król, E.; Białas, A. Axial Flux Permanent Magnet Motors as drive slow moving vehicles—Review of construction. *Przegląd Elektrotechniczny* **2011**, *87*, 1–4.
9. Lovatt, H.C.; Elton, D.; Cahill, L.; Hau, H.D.; Stumpf, A.; Kulkarni, A.; Kapoor, A.; Ektesabi; Mazumder, H.; Dittmar, T.; et al. Design procedure for low cost, low mass, direct drive, in-wheel motor drivetrains for electric and hybrid vehicles. In Proceedings of the IECON 2011—37th Annual Conference on IEEE Industrial Electronics, Melbourne, VIC, Australia, 7–10 November 2011.
10. Lovatt, H.C.; Ramsden, V.S.; Mecrow, B.C. Design of an in-wheel motor for a solar powered electric vehicle. *Electr. Power Appl. IEE Proc.* **1998**, *145*, 402–408. [[CrossRef](#)]
11. Terashima, M.; Ashikaga, T.; Mizuno, T.; Natori, K.; Fujiwara, N.; Yada, M. Novel motors and controllers for high-performance electric vehicle with four in-wheel motors. *IEEE Trans. Ind. Electron.* **1997**, *44*, 28–38. [[CrossRef](#)]
12. Alibeik, M.; Santos, E.C. High-Torque Electric Machines: State of the Art and Comparison. *Machines* **2022**, *10*, 636. [[CrossRef](#)]
13. Zhu, Z.Q.; Howe, D. Electrical Machines and Drives for Electric, Hybrid, and Fuel Cell Vehicles. *Proc. IEEE* **2007**, *95*, 746–765. [[CrossRef](#)]
14. Mizutani, R.; MATSUI, N. Optimum Design Approach for Low-Speed, High-Torque Permanent Magnet Motors. *Electr. Eng. Jpn.* **2001**, *135*, 52–63. [[CrossRef](#)]
15. Chen, Q.P. Study on temperature influence factors and electromagnetic heat coupling of in-wheel motor for micro-electric vehicle. *Mechanika* **2014**, *20*, 80–86. [[CrossRef](#)]
16. Chong, Y.; Subiabre, E.J.P.E.; Mueller, M.A.; Chick, J.; Staton, D.A.; McDonald, S.A. The Ventilation Effect on Stator Convective Heat Transfer of an Axial-Flux Permanent Magnet Machine. *IEEE Trans. Ind. Electron.* **2014**, *61*, 4392–4403. [[CrossRef](#)]
17. Dorrell, G.D.; Staton, D.A.; Hahout, J.; Hawkins, C.; McGilp, M.I. Linked electromagnetic and thermal modelling of a permanent magnet motor. In Proceedings of the 3rd IET International Power Electronics, Machines and Drives, Dublin, Ireland, 4–6 April 2006.
18. Ge, Y.; Wang, S.G. Analysis and calculation of stator temperature field of permanent magnet brushless DC motor for electric bicycle. *Micromotors Servo Tech.* **2008**, *41*, 5–8.
19. Jakubowski, R.; Szcypior, J. Układ chłodzenia i obliczenia cieplne maszyny z wirnikiem zewnętrznym. *Prace Nauk. Inst. Masz. Napędów i Pomiarów Elektr. Politech. Wrocławskiej* **2012**, *66*, 408–417.
20. Nerg, J.; Rilla, M.; Pyrhönen, J. Thermal analysis of radial-flux electrical machines with a high power density. *IEEE Trans. Ind. Electron.* **2008**, *55*, 3543–3554. [[CrossRef](#)]
21. Mynarek, P. Analiza Stanów Ciepłych w Silnikach Małej Mocy. Ph.D. Thesis, Politechnika Opolska, Opole, Poland, 2014.
22. Będkowski, B. System Doboru i Oceny Parametrów Układów Chłodzenia Wybranych Maszyn Elektrycznych. Ph.D. Thesis, Akademia Techniczno-Humanistyczna, Bielsko-Biała, Poland, 2015.
23. Mynarek, P.; Kowol, M. Analiza Ciepłota Silnika PMSM za Pomocą Metody Elementów Skończonych oraz Schematów Ciepłych. *Zesz. Probl. Masz. Elektr.* **2014**, *104*, 49–54.
24. Fasil, M.; Plesner, D.; Walther, J.H.; Mijatovic; Holbøll, J.; Jensen, B.B. Numerical and Experimental Investigation of Heat Flow in Permanent Magnet Brushless DC Hub Motor. *SAE Int. Am. Univ. Beirut* **2015**, *4*, 46–57. [[CrossRef](#)]
25. Staton, D.; Chong, E.; Pickering, S.; Boglietti, A. *Cooling of Rotating Electrical Machines Fundamentals, Modeling, Testing and Design*; IET Energy Engineering Series; IET: Stevenage, UK; Volume 109.
26. Howe, Z.Q.Z.a.D. Influence of design parameters on cogging torque in permanent magnet machines. *IEEE Trans. Energy Convers.* **2000**, *15*, 407–412.
27. Chen, Q.; Shu, H.; Chen, L.; Chen, B. Analysis on cogging torque of driving in-wheel motor for electric vehicle. *Int. J. Electr. Hybrid Veh.* **2012**, *4*, 148–160. [[CrossRef](#)]
28. Kim, I.-W.; Woo, D.-K.; Yeo, H.-K.; Jung, H.-K. Cogging torque optimization of in-wheel type motor based on gradient assisted simplex method. In Proceedings of the Vehicle Power and Propulsion Conference (VPPC), Seoul, Republic of Korea, 9–12 October 2012.

29. Hwang, M.-H.; Lee, H.-S.; Cha, H.-R. Analysis of Torque Ripple and Cogging Torque Reduction in Electric Vehicle Traction Platform Applying Rotor Notched Design. *Energies* **2018**, *11*, 3053. [CrossRef]
30. Petkovska, L.; Lefley, P.; Cvetkovski, G. Design techniques for cogging torque reduction in a fractional slot PMSM motor. *COMPEL Int. J. Comput. Math. Electr. Electron. Eng.* **2020**, *39*, 1041–1055. [CrossRef]
31. Gong, H.; Chai, F.; Pei, Y.; Cheng, S. Research on torque performance for permanent magnet in wheel motor. In Proceedings of the Vehicle Power and Propulsion Conference, Harbin, China, 3–5 September 2008. [CrossRef]
32. Goryca, Z.; Ziółek, M.; Malinowski, M. Moment Zaczepowy Wielobiegowej Maszyny. *Zesz. Probl.-Masz. Elektr.* **2010**, *88*, 53–56.
33. Ma, G.; Qiu, X.; Jianfei, Y.; Bu, F. Structural Parameter Optimization to Reduce Cogging Torque of the Consequent Pole In-Wheel Motor. In Proceedings of the 2018 IEEE 18th International Power Electronics and Motion Control Conference (PEMC), Budapest, Hungary, 26–30 August 2018. [CrossRef]
34. Młot, A.; Łukaniszyn, M. Optimization of the PM array of brushless DC motor for minimum cogging torque. *Przegląd Elektrotechniczny* **2008**, *84*, 169–174.
35. Ślaski, G.; Gudra, A.; Borowicz, A. Analysis of the influence of additional unsprung mass of in-wheel motors on the comfort and safety of a passenger car. *Arch. Automot. Eng.* **2014**, *65*, 51–64.
36. Parczewski, K.; Romaniszyn, K.; Wnęk, H. Influence of electric motors assembly in hubs of vehicle wheels on the dynamics of movement, especially on surfaces with different adhesion coefficient. *Combust. Eng.* **2019**, *58*, 58–64. [CrossRef]
37. Dukalski, P.; Będkowski, B.; Parczewski, K.; Wnęk, H.; Urbaś, A.; Augustynek, K. Analysis of the influence of assembly electric motors in wheels on behaviour of vehicle rear suspension system. *Mater. Sci. Eng.* **2018**, *421*, 022004. [CrossRef]
38. Dukalski, P.; Będkowski, B.; Parczewski, K.; Wnęk, H.; Urbaś, A.; Augustynek, K. Dynamics of the vehicle rear suspension system with electric motors mounted in wheels. *Maint. Reliab.* **2019**, *21*, 125–136. [CrossRef]
39. Frajnkovic, Omerovic, S.; Rozic, U.; Kern, J.; Connes, R.; Renner, K.; Biček, M. Structural Integrity of In-Wheel Motors. *SAE Tech. Pap.* **2018**, 1829. [CrossRef]
40. Biček, M.; Connes, R.; Omerović, S.; Gündüz, A.; Kunc, R.; Zupan, S. The Bearing Stiffness Effect on In-Wheel Motors. *Sustainability* **2020**, *12*, 4070. [CrossRef]
41. Parczewski, K.; Wnęk, H. Comparison of overcoming inequalities of the road by a vehicle with a conventional drive system and electric motors placed in the wheels. In Proceedings of the Conference Transport Means, Kaunas, Lithuania, 30 September–2 October 2020.
42. Li, G.; Wang, Y.; Zong, C. Driving State Estimation of Electric Vehicle with Four Wheel Hub Motors. *Qiche Gongcheng. Automot. Eng.* **2018**, *40*, 150–155.
43. Wanner, D.; Kreusslein, M.; Augusto, B.; Drugge, L. Single wheel hub motor failures and their impact on vehicle and driver behavior. *Veh. Syst. Dyn.* **2016**, *54*, 1345–1361. [CrossRef]
44. Watts, A.; Hilton, C.; Fraser, A.; Anderson, M.; Harty, D. “Unsprung Mass” The Myths and Realities—Closing the Circle; SAE International: Warrendale, PA, USA, 2011.
45. Anderson, M.; Harty, D. Unsprung Mass with In-Wheel Motors—Myths and Realities. Presented at the Society of Automotive Engineers, 2011. Available online: <https://www.proteanelectric.com/f/2018/04/protean-Services3.pdf> (accessed on 19 October 2023).
46. Schalkwyk, D.J.V.; Kamper, M.J. Effect of Hub Motor Mass on Stability and Comfort of Electric Vehicles. In Proceedings of the 2006 IEEE Vehicle Power and Propulsion Conference, VPPC '06, Windsor, UK, 6–8 September 2006.
47. Nagaya, G.; Wakao, Y.; Abe, A. Development of an in-wheel drive with advanced dynamic-damper mechanism. *JSAE* **2003**, *24*, 477–481. [CrossRef]
48. Johansen, P.; Pattersib, D.; Oykkeefe, C. The use of an axial flux permanent magnet in-wheel direct drive in an electric bicycle. *Renew. Energy* **2001**, *22*, 151–157. [CrossRef]
49. Yang, Y.P.; Luh, Y.P.; Cheng, C.H. Design and control of axial flux brushless DC wheel motors for electric vehicles-part I: Multi-objective optimal design and analysis. *IEEE Trans. Magn.* **2004**, *40*, 1873–1882. [CrossRef]
50. Tianze, S. *Design and Performance Matching of Wheel Hub Motor Drive Electric Vehicle Suspension and Steering System*; Jilin University: Changchun, China, 2015.
51. Di, T. *Dynamic Characteristics and Structural Optimization of Wheel Hub Motor Drive System with Built-in Suspension*; South China University of Technology: Guangzhou, China, 2013.
52. Wang, R.; Chen, Y.; Feng, D. Development and performance characterization of an electric ground vehicle with independently actuated in-wheel motors. *J. Power Sources* **2011**, *196*, 3962–3971. [CrossRef]
53. Sun, Y.; Li, M.; Liao, C. Analysis of Wheel Hub Motor Drive Application in Electric Vehicles. In Proceedings of the MATEC Web of Conferences, Zurich, Switzerland, 19–21 October 2015. [CrossRef]
54. Dukalski, P. A System of Construction Solutions for Designing Electric Motors with Increased Power Density for Electromobility Applications. Ph.D. Thesis, Silesian University of Technology, Gliwice, Poland, 2024.
55. Dukalski, P.; Krok, R. Selected Aspects of Decreasing Weight of Motor Dedicated to Wheel Hub Assembly by Increasing Number of Magnetic Poles. *Energies* **2021**, *14*, 917. [CrossRef]
56. Manual Motor-CAD. nr v14.1. Available online: <https://www.scribd.com/document/399317241/Manual-Motorcad> (accessed on 12 November 2022).
57. Kowal, D.; Sergeant, P.; Dupré, L.; Vandenbossche, L. Comparison of Iron Loss Models for Electrical Machines with Different Frequency Domain and Time Domain Methods for Excess Loss Prediction. *IEEE Trans. Magn.* **2015**, *51*, 6300110. [CrossRef]

58. Yamazaki, K.; Fukushima, N. Iron-Loss Modeling for Rotating Machines: Comparison Between Bertotti's Three-Term Expression and 3-D Eddy-Current Analysis. *IEEE Trans. Magn.* **2010**, *46*, 3121–3124. [[CrossRef](#)]
59. Zhao, H.; Luo, Y.; Wang, H.; Peter, B. A Complete Model for Iron Losses Prediction in Electric Machines Including Material Measurement. FE Computation and Experimental Validation Electrical Review. *Przegląd Elektrotechniczny* **2012**, *88*, 52–55.
60. Bertotti, G. General properties of power losses in soft ferromagnetic materials. *IEEE Trans. Magn.* **1988**, *24*, 621–630. [[CrossRef](#)]
61. Roshandel, G.; Mahmoudi, E.; Kahourzade, A.; Yazdani, S.; Shafiullah, A. Losses in Efficiency Maps of Electric Vehicles. *Energies* **2021**, *14*, 7805. [[CrossRef](#)]
62. Park, G.J.; Son, B.; Jung, S.Y.; Kim, Y.J. Reducing computational time strategy for estimating coreloss with spatial and temporal periodicity. In Proceedings of the 2016 IEEE Transportation Electrification Conference and Expo, Asia-Pacific (ITEC Asia-Pacific), Busan, Korea, 1–4 June 2016.
63. Dąbrowski, M. *Projektowanie Maszyn Elektrycznych Prądu Przemiennej*; WNT: Warszawa, Poland, 1988.
64. Śliwiński, T. *Metody Obliczania Silników Indukcyjnych, t.1 Analiza*; PWN: Warszawa, Poland, 2008.
65. Ruoho, S.; Santa-Nokki, T.; Kolehmainen, J.; Arkkio, A. Modeling Magnet Length In 2-D Finite-Element Analysis of Electric Machines. *IEEE Trans.* **2009**, *45*, 3114–3120. [[CrossRef](#)]
66. Wrobel, P.M.R. A General Cuboidal Element for Three-Dimensional Thermal Modelling. *IEEE Trans. Magn.* **2010**, *46*, 3197–3200. [[CrossRef](#)]
67. Liu, Y.; Martinet, S.; Louis, C.; Pasquier, A. Emission Characterization of In-Use Diesel and Gasoline Euro 4 to Euro 6 Passenger Cars Tested on Chassis Dynamometer Bench and Emission Model Assessment. *Aerosol. Air Qual. Res.* **2017**, *17*, 2289–2299. [[CrossRef](#)]
68. Michel, A. The ARTEMIS European driving cycles for measuring car pollutant emissions. *Sci. Total Environ.* **2005**, *334*, 73–84. [[CrossRef](#)]
69. Nyberg, P.; Frisk, E.; Nielsen, L. Using Real-World Driving Databases to Generate Driving Cycles with Equivalence Properties. *IEEE Trans. Veh. Technol.* **2015**, *65*, 4095–4105. [[CrossRef](#)]
70. Toda, H.; Xia, Z.; Wang, J. Rotor Eddy-Current Loss in Permanent Magnet Brushless Machines. *IEEE Trans. Magn.* **2004**, *40*, 2104–2106. [[CrossRef](#)]
71. Soong, W.L.; Ertugrul, N. Field-Weakening Performance of Interior Permanent-Magnet Motors. *IEEE Trans. Ind. Appl.* **2002**, *38*, 1251–1258. [[CrossRef](#)]
72. Wolnik, T.; Styskala, V.; Mlcak, T. Study on the Selection of the Number of Magnetic Poles and the Slot-Pole Combinations in Fractional Slot PMSM Motor with a High Power Density. *Energies* **2021**, *15*, 215. [[CrossRef](#)]
73. Sun, T.; Kim, J.M.; Lee, G.H.; Hong, J.P.; Choi, M.R. Effect of pole and slot combination on noise and vibration in permanent magnet synchronous motor. *IEEE Trans. Magn.* **2011**, *47*, 1038–1041. [[CrossRef](#)]
74. Wang, C.C.; Wu, H.M.; Cheng, S.P. Influence of pole and slot combinations on cogging torque in fractional slot PM motors. *J. Magn. Magn. Mater.* **2006**, *30*, e430–e432. [[CrossRef](#)]
75. Demir, Y.; EL-Refaie, A.M.; Aydin, M. Investigation of Asymmetric and Unbalanced Winding Structures for 3-Phase Permanent Magnet Synchronous Machines. *IEEE Trans. Energy Convers.* **2021**, *36*, 1722–1732. [[CrossRef](#)]

Disclaimer/Publisher's Note: The statements, opinions and data contained in all publications are solely those of the individual author(s) and contributor(s) and not of MDPI and/or the editor(s). MDPI and/or the editor(s) disclaim responsibility for any injury to people or property resulting from any ideas, methods, instructions or products referred to in the content.